



POLITECNICO
MILANO 1863

SCUOLA DI INGEGNERIA INDUSTRIALE
E DELL'INFORMAZIONE

Characterization of PAGAT polymeric gel for Hadron Therapy dosimetry

TESI DI LAUREA MAGISTRALE IN
NUCLEAR ENGINEERING-INGEGNERIA NUCLEARE

Author: **Riccardo Brambilla**

Student ID: 964355
Supervisor: Prof. Mario Mariani
Co-supervisor: Dr. Gabriele Magugliani
Academic Year: 2022-2023

Contents

Contents	i
Abstract.....	iii
Estratto.....	v
1. Chemical gel dosimetry.....	3
1.1 Introduction	3
1.2 Polymer gel dosimeters	8
1.2.1 Water radiolysis	10
1.2.2 Polymerization mechanism	13
1.2.3 PAGAT dosimeter.....	19
1.3 Dosimeter analysis	23
1.3.1 Spectrophotometric analysis	24
1.3.2 MRI analysis	27
2. Hadron Therapy.....	38
2.1 Introduction	38
2.1.1 Physical properties of Hadrons	44
2.1.2 Radiobiological properties of carbon ions.....	50
2.2 Gel dosimetry in Hadron Therapy	53
3. Materials and methods.....	59
3.1 Gel preparation.....	59
3.2 Irradiation.....	61
3.3 Dosimeter analysis	64
3.3.1 Spectrophotometric analysis	64
3.3.2 MRI analysis	65
3.4 Data analysis	68
4. Results and discussion	70
4.1 Characterization	70
4.1.1 Spectrophotometric analysis	71
4.1.2 MRI analysis	73

4.2 Volumetric response	76
5. Conclusion and future development.....	84
Bibliography.....	87
List of Figures.....	97
List of Tables	101
List of Acronyms.....	103

Abstract

The general principle of radiotherapy consists in delivering high radiation doses to tumoral tissue to destroy or inactivate malign cells following DNA damage. In order to spare the healthy tissue, the delivered dose distribution needs to be conformal to the tumor target and characterized by a very high spatial accuracy and precision. Modern radiotherapy relies on dedicated Treatment Planning System (TPS) software whose calculations need to be validated and verified experimentally prior to actual delivery.

With the advent of highly conformal radiotherapy, dosimetry has become even more important in the process of quality assurance (QA) and treatment plan verification. Conventional devices, such as ionization chambers or radiochromic films, have however important limitations due to their 1D or 2D nature which provides only a partial sampling of the whole distributions reducing the measurement resolution. Moreover, most conventional dosimeters are not radiologically tissue equivalent, requiring the application of correction factors to convert the detector measurement to an absorbed dose to the patient.

Chemical gel dosimeters are good candidates to improve on these limitations and provide a quantitative 3D dose map for QA pre-treatment dosimetry. The ability of directly measuring complex 3D dose distributions, radiological tissue equivalence and high spatial resolution are among the main promising properties of these dosimeters. Two categories of chemical gel dosimeters can be identified: radiochromic gel dosimeters and polymer gel dosimeters. This thesis work focuses on the characterization of the PAGAT dosimeter, consisting of a polyacrylamide hydrogel with THPC as antioxidant, and investigated its use in Hadron Therapy (HT) dosimetry.

HT is a kind of radiotherapy which makes use of accelerated hadrons for the treatment of surgically inoperable or radioresistant tumors. Due to their physical and radiobiological properties, hadrons allow the achievement of a more conformal dose deposition compared to conventional types of radiotherapy, better sparing healthy tissues located around the tumor. Throughout this thesis work, the irradiation session was conducted using monoenergetic proton and carbon ion beams generated by the 25-metre diameter synchrotron accelerator at CNAO (Centro Nazionale di Adroterapia Oncologica) facility in Pavia (Italy).

The characterization phase aimed at verifying a linear dose response and calculate dosimetric parameters at different irradiation conditions. Spectrophotometric cuvettes were uniformly irradiated using monoenergetic protons and carbon ions up to 4 Gy. The dosimeter readout was accomplished via spectrophotometric and Magnetic Resonance Imaging (MRI) measurements, and a good linearity for all investigated doses and temporal stability up to more than two months was confirmed.

Volumetric dose mapping was performed using cylindrical phantoms irradiated with proton and carbon ion single-spot beams. Dose deposition was measured using MRI analysis and depth-dose curves and transversal dose distributions were compared to reference profiles. An underestimation of the dose response in the Bragg peak region due to high-LET quenching effect was confirmed in accordance with literature results. The study also found that PAGAT gels could be used for relative dosimetry measurements as the geometrical information of the dose deposition was successfully recorded.

Key-words: PAGAT gel dosimeter, spectrophotometry, MRI, Hadron Therapy, proton beam, carbon ion beam.

Estratto

La radioterapia oncologica si basa sul principio di fornire alte dosi di radiazioni al tessuto tumorale per distruggerne o inattivarne le cellule a seguito di danni al DNA. Per non intaccare il tessuto sano, la dose somministrata deve avere una distribuzione il più possibile conforme al bersaglio individuato e deve essere caratterizzata da una precisione e accuratezza spaziale molto elevate. La radioterapia moderna si serve di software per la pianificazione del trattamento i cui calcoli devono essere validati e verificati sperimentalmente prima dell'effettiva somministrazione.

Con l'avvento della radioterapia conformazionale, la dosimetria è diventata ancora più importante nel processo di garanzia di qualità e verifica del piano di trattamento. Tuttavia, i dispositivi convenzionali come le camere a ionizzazione o i film radiocromici presentano importanti limitazioni dovute alla loro natura 1D o 2D, la quale fornisce solo un campionamento parziale delle distribuzioni di dose riducendo la risoluzione delle misurazioni. Inoltre, la maggior parte dei dosimetri convenzionali non è tessuto equivalente, richiedendo l'applicazione di fattori correttivi per convertire la misurazione in dose assorbita dal paziente.

I dosimetri chimici a gel si presentano come buoni candidati per superare queste limitazioni e fornire una mappatura di dose tridimensionale per la dosimetria di pretrattamento. La capacità di misurare direttamente distribuzioni tridimensionale complesse, la tessuto-equivalenza e l'alta risoluzione spaziale sono tra le proprietà più promettenti. È possibile identificare due categorie di dosimetri chimici a gel: i dosimetri a gel radiocromici e i dosimetri a gel polimerici. Questo lavoro di tesi si concentra sulla caratterizzazione del dosimetro PAGAT, composto da un idrogel di poliacrilammide con THPC come antiossidante, e si è indagato il suo utilizzo nella dosimetria in ambito di adroterapia.

L'adroterapia è una forma di radioterapia che utilizza adroni per il trattamento di tumori chirurgicamente inoperabili o radioresistenti. Grazie alle loro proprietà fisiche e radiobiologiche, gli adroni consentono di ottenere una deposizione di dose più conforme rispetto a metodi convenzionali riuscendo maggiormente a non intaccare i tessuti sani vicini al tumore. Nel corso di questo lavoro di tesi, la sessione di irraggiamento è stata condotta utilizzando fasci monoenergetici di protoni e ioni carbonio generati dal sincrotrone da 25 metri di diametro dello CNAO (Centro Nazionale di Adroterapia Oncologica) a Pavia.

La fase di caratterizzazione aveva lo scopo di verificare una risposta lineare alla dose e calcolare i parametri dosimetrici in diverse condizioni di irraggiamento. Cuvette spettrofotometriche sono state irraggiate uniformemente utilizzando fasci monoenergetici di protoni e ioni carbonio fino a 4 Gy. La lettura dei dosimetri è stata effettuata tramite misure spettrofotometriche e risonanza magnetica, confermando una buona linearità per le dosi esaminate e una stabilità temporale oltre i due mesi.

La mappatura volumetrica di dose è stata effettuata utilizzando fantocci cilindrici irraggiati con fasci puntuali di protoni e ioni carbonio. La deposizione di dose è stata misurata utilizzando analisi di risonanza magnetica e le curve di dose in profondità e le distribuzioni trasversali sono state confrontate con profili di riferimento. È stata confermata una sottostima della dose nella regione del picco di Bragg a causa dell'effetto di quenching ad alto LET, in accordo con i risultati presenti in letteratura. Lo studio ha inoltre evidenziato che i gel PAGAT possono essere utilizzati per misurazioni dosimetriche relative in quanto le informazioni geometriche della deposizione di dose sono state registrate con successo.

Parole chiave: dosimetri a gel PAGAT, spettrofotometria, IRM, adroterapia, fascio di protoni, fascio di ioni carbonio.

1. Chemical gel dosimetry

In this chapter, an overview on chemical gel dosimetry will be presented. Starting from the basis of dosimetry in radiotherapy, the main limitations of conventional dosimeters will be discussed alongside introducing the principal advantages in using radiosensitive gels for 3D dose mapping. Focusing on polymer gel dosimeters, particular attention will be given to the process of polymerization, from water radiolysis to the role of oxygen as inhibitor and the need of its sequestration.

At the end of the chapter, the main techniques for polymer gel dosimeter readout will be addressed outlining the working principles behind them.

1.1 Introduction

According to the WHO Global Cancer Observatory, considering the increase in world population and life expectancy, the estimated number of new cancer cases per year will almost double between 2020 and 2040 [1]. Together with surgery and chemotherapy, radiotherapy is one of the most effective techniques used today for the treatment of cancers. Due to its efficiency and the possibility to be combined with other techniques, the proportion of oncological patients who should receive radiotherapeutic treatments is over 50% [2]. Though many kinds of radiotherapy technologies are now available, the general principle consists in delivering high radiation doses to the tumoral tissue and exploiting the ability of ionizing radiation to destroy or inactivate cells through biological effects following DNA damage [3], [4]. In

order to spare the healthy tissue and prevent the formation of secondary tumors, the dose distribution needs to be characterized by a very high spatial precision. For this purpose, before the treatment it is essential to have diagnostic techniques able to localize the tumor target with a sufficient spatial resolution.

Nowadays, using imaging techniques such as Magnetic Resonance Imaging (MRI), Transmission Computed Tomography (TCT), Positron Emission Tomography (PET) and hybrid technologies (i.e. PET/CT, PET/MRI), it is possible to achieve sub-mm resolution in the definition of the target volume [5]–[8]. This high spatial resolution of the imaging technique needs to be met by high spatial accuracy and precision of the dose delivery system in the radiotherapeutic session to obtain local disease control and limited side effects.

Modern radiotherapy employs different methods to conform the dose distribution to the desired target volume, using beam collimation (i.e. Intensity-Modulated Radiation Therapy IMRT), exploiting the ballistic precision of beam particles (Hadron Therapy HT) or limited range of radiation emitted by a sealed source (Brachytherapy) [9]. For all these techniques, using the data collected during the diagnostic session, it is crucial to develop a dedicated Treatment Planning System (TPS), through which a simulation of the irradiation in a specific point of the patient's body is performed and optimized. These TPS are very complex model-based software, some of them implementing Monte Carlo (MC) calculation algorithms, whose predictions need to be validated and verified experimentally. Based on TPS outputs, practitioners set parameters such as fluence distribution, particle energy, gantry angle, collimators position, to achieve the desired dose distribution [10], [11].

With the advent of conformal radiotherapy, dosimetry has become even more important in the process of quality assurance (QA) and treatment plan verification. Consistency in dose delivery, volume definition and reproducibility of the dose output

are paramount and need to be benchmarked experimentally [12]. The need for dosimetric verification in clinical application can be attributed to three main reasons: first, the possibility of discrepancies between the calculated dose distribution and the actual given one; second, occurrence of machine failures or drifts which may lead to inaccurate delivery; third, detection of set-up errors [13]. Dosimeters are therefore employed to perform such verifications.

A dosimetric system must meet several essential criteria to be considered a functional dosimetric device. These characteristics can be listed as follows [14]:

1. Dose response should be measurable, accurate and reliable.
2. Dose measurement should have high dose resolution.
3. Dose response should be stable, that is it does not change in time.
4. Dose response should be ideally linear over a sufficient dose range.
5. Dose response should not be susceptible to environmental factors that may vary during operation, such as temperature, pressure or atmospheric gases.
6. Dosimeter should express very good tissue equivalence for the kind of radiation and energies it is used for.
7. Dependencies of the dose response on radiation energy and dose-rate should be as small as possible.
8. Dose result should be characterized by reproducibility.

In practice, no dosimeter meets all of these criteria, but nonetheless some systems have more desirable characteristics than others.

One-dimensional dosimeters, such as ionization chambers, semiconductor diodes or thermoluminescent dosimeters (TLD), can be used for point-dose measurements. They can verify monitor unit outputs in homogeneous dose regions but cannot directly measure beam profiles or dose distributions with high resolution

due to volume averaging related to pair creation in the active volume [15], [16]. Radiochromic films, diode arrays or ionization chamber arrays are currently used for two-dimensional dosimetry, allowing to obtain 2D dose maps at a given irradiation depth [15]. Measurements of beam profile and beam penumbra are possible, and a 3D map can be computationally reconstructed by back-projecting different planar distributions [17]. These methods have however important limitations [18]. The 2D nature provides only a partial sampling of the whole distributions reducing the measurement resolution and small volume detectors in 2D arrays are subject to volume effect perturbations. When it comes to high dose gradients and complex dose distributions, full 3D dosimetry capacity is highly desirable. Moreover, most conventional dosimeters are not radiologically tissue equivalent, requiring the application of correction factors to convert the detector measurement to an absorbed dose to the patient [19].

Chemical gel dosimeters are good candidates to improve on these limitations and provide a quantitative 3D dose map for QA pre-treatment dosimetry [20]. Besides the ability of directly measuring complex 3D dose distributions and their radiological tissue equivalence, gel dosimeters have other favorable properties compared to conventional devices which can simplify radiotherapy dosimetry, namely radiation direction independence (response isotropy), high spatial resolution and integration of dose during treatment [21]. Two categories of chemical gel dosimeters can be identified: radiochromic gel dosimeters and polymer gel dosimeters [22]. This thesis work focuses on the latter category.

Both radiochromic and polymer gel dosimeters belong to the family of chemical dosimeters, which work by measuring radiation-induced chemical transformations whose magnitude is proportional to the absorbed dose. The most widely used and best studied among the chemical devices is the Fricke standard dosimeter. It is a liquid

radiochromic dosimeter developed in 1927 by Fricke and Morse exploiting a ferrous sulfate solution, known today as Fricke solution [23]. The dosimetric basis is provided by the oxidation upon irradiation of ferrous (Fe^{2+}) ions to ferric (Fe^{3+}) ions [24]. The quantity of Fe^{3+} produced depends on the energy absorbed by the solution and therefore by measuring the change in ferric ions concentration it is possible to obtain the absorbed dose, by [25]:

$$D = \frac{N_A \cdot e}{100\rho \cdot G(Fe^{3+})} \cdot \Delta[Fe^{3+}] \quad (1.1)$$

where D is the absorbed dose in Gy, ρ is the density in kg/L, $G(Fe^{3+})$ is the chemical yield of Fe^{3+} expressed in ions produced per 100 eV, N_A is the Avogadro number, e is the charge of the electron in J/eV and $\Delta[Fe^{3+}]$ is the resultant change in ferric ion concentration in mol/L. Upon careful and standardized preparation of aqueous Fricke solution, the ferric ion chemical yield $G(Fe^{3+})$ is well characterized and equal to 15.6 $Fe^{3+}/100$ eV, hence the Fricke dosimeter has the advantage of being an absolute dosimeter without requirement for calibration [25]. Its main disadvantage is given by its liquid nature, which makes it impossible to record a spatial information of the dose distribution.

In 1984 Gore *et al* proposed adding gelling agents to the Fricke solution to stabilize the geometric dose information into a gel matrix and demonstrated that 3D dose distributions could be recorded and readout using MRI [22], [26]. The conventional term for ferrous sulfate doped gel is Fricke gel dosimeter. The dosimetric response of these gel dosimeters is still based on Eq. (1.1), but the chemical yield is increased from the aqueous Fricke value due to the addition of chemical pathways for the conversion of Fe^{2+} provided by the gel macromolecules [27]. Notable advantages of the Fricke gels, besides the spatial dose determination, are high sensitivity, simple

fabrication, consistent reproducibility and radiological water and tissue equivalence [28], [29]. These devices are however affected by diffusion of the radio-induced products which in time destroys the spatial information for which even the use of Fe^{3+} chelating agents, such as xylenol orange, has only limited success [30].



Figure 1. Photograph of Fricke gel dosimeters irradiated up to 30 Gy at 5 Gy increments [31].

1.2 Polymer gel dosimeters

In 1992 a new gel dosimeter formulation was proposed by Maryanski *et al* based on the polymerization of acrylamide (AAm) and N,N' -methylene-bis-acrylamide (Bis) monomers infused in an aqueous agarose matrix [32]. This system was given the acronym BANANA due its chemical components (bis, acrylamide, nitrous oxide and agarose) [33]. The BANANA polymer gel dosimeter did not show the diffusion problem associated with Fricke gels and was found to have a relatively stable post-irradiation dose distribution [34]. In 1994 Maryanski *et al* refined the formulation by replacing agarose with gelatin and the polymer gel dosimeter acronym of choice for most authors subsequently became PAG (polyacrylamide gel) [35], [36]. Due to the nature the polymerization chemistry, polymer gel dosimeters were susceptible to atmospheric oxygen inhibition [34]. As a result, PAG-type devices had to be manufactured in an oxygen-free environment, such as a glove box pumped with

nitrogen gas [36]. Along with the use of potentially toxic chemicals [37], this was a significant limitation in the introduction of gel dosimetry in clinical applications.

With the development by Fong *et al* in 2001 of a new type of polymer gel dosimeter, known as MAGIC, in which atmospheric oxygen was bound in metallo-organic complex, the oxygen inhibition problem was mitigated enabling to greatly simplify the manufacturing process [38]. The MAGIC polymer gel formulation consisted of methacrylic acid (MAA), ascorbic acid (AscA), gelatin and copper. The principle behind the MAGIC oxygen removal was to use as antioxidant ascorbic acid, which bound free oxygen contained within the aqueous gelatin matrix into metallo-organic complexes in a process initiated by copper sulfate [39]. These types of antioxidant-doped polymer gels were named normoxic gel dosimeters, to distinguish them from the previous formulations which became known as hypoxic or anoxic. Afterwards, numerous compositions and formulations for normoxic polymer gel dosimeters were studied and some of them are summarized in Table 1. In 2002, De Deene *et al* showed that tetrakis (hydroxymethyl) phosphonium chloride (THPC) could be used as antioxidant and in 2004 THPC was added and investigated in the PAG formulation by Venning *et al*: the resulting normoxic dosimeter type is now known with the acronym PAGAT (polyacrylamide gel and THPC) [39], [40]. This thesis work focuses on the study of PAGAT polymer gel dosimeter, whose samples are shown in Figure 2.



Figure 2. Photograph of PAGAT polymer gels irradiated at increasing doses from left to right.

Table 1. Different formulations for normoxic gel dosimeters [41].

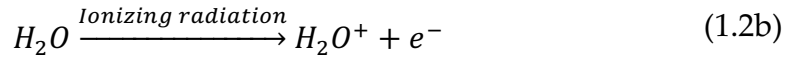
<i>Normoxic dosimeter</i>	<i>Composition</i>
MAGIC (2001)	Methacrylic acid, ascorbic acid, hydroquinone, CuSO ₄ ·5H ₂ O, gelatin
MAGAS (2002)	Methacrylic acid, ascorbic acid, gelatin
MAGAT (2002)	Methacrylic acid, tetrakis (hydroxymethyl) phosphonium chloride, gelatin
nMAG (2006)	Methacrylic acid, Bis [tetrakis (hydroxymethyl) phosphonium] sulfate, gelatin
PAGAS (2002)	Acrylamide, N,N-methylene-bis-acrylamide, Ascorbic acid, gelatin
PAGAT (2004)	Acrylamide, N,N-methylene-bis-acrylamide, tetrakis (hydroxymethyl) phosphonium chloride, hydroquinone, gelatin
nPAG (2006)	Acrylamide, N,N-methylene-bis-acrylamide, Bis [tetrakis (hydroxymethyl) phosphonium] sulfate, gelatin

Fundamental principles of polymer gel chemistry will be addressed in the next sections before moving to the techniques employed for the dosimeters analysis.

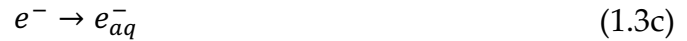
1.2.1 Water radiolysis

The types of gels used in gel dosimeters are characterized by a high content of water, of the order of 90%, and for this reason they are also referred to as hydrogels [34]. In particular, the PAGAT dosimeter contains 89% weight percentage of water. The residual mass is predominantly organic materials such as gelatin and monomers [22]. As such, upon irradiation dose is deposited primarily to water molecules leading to their dissociation in radicals and ions in a process known as water radiolysis [42]. The solute is therefore often not affected directly by the radiation but only indirectly by chemically interacting with highly reactive radiolytic products.

When ionizing radiation directly interacts with matter, this latter will absorb the energy through excitation or ionization of particles along the radiation track. In the case of a pure water system, the interactions can be described as follows [42]:



These excited and ionized species will de-excite and, by subsequently diffusing outside of the track, will interact with the other molecules to form radiolytic products. Some of the main reactions are the following [42]:



To summarize, the main radiolytic products arising from pure water radiolysis are free radicals, such as hydrogen radical H^\bullet and hydroxyl radical OH^\bullet , ionic species, such as hydrated electron e_{aq}^- , hydrogen ion H^+ and hydroxyl ion OH^- or new stable species, such as oxygenated water H_2O_2 and hydrogen molecule H_2 .

What described so far is true for a pure water system, but generally some impurities in the form of oxygen molecules O_2 or nitrogen molecules N_2 may also be dissolved among H_2O molecules. The presence of oxygen is particularly important since O_2 plays the role of radical scavenger and can react with radiolytic products

creating peroxide radicals which are responsible for polymerization inhibition. Hydrogels prepared at room temperature and exposed to the air will contain approximately 1 mM of oxygen [22]. In this case, during water radiolysis, due to the occurrence of scavenging reactions with O_2 , new species are formed such as HO_2^\bullet and $O_2^{\bullet-}$ while others, like e_{aq}^- and H^\bullet , are absent [42]:



Radiolytic products are often subdivided into reducing products (e_{aq}^- and H^\bullet) and oxidizing products (OH^\bullet , HO_2^\bullet and H_2O_2) since the two groups tend to bring about reduction and oxidation of inorganic solutes, respectively; molecular hydrogen is relatively inert and plays little part in subsequent reactions [42].

The radiochemical yields of these water radiolytic products depend on several factors: type of radiation, water pH, scavenger (such as free oxygen) concentration, water temperature and absorbed dose rate [43], [44]. Some values of radiochemical yields (expressed in number of particles per 100 eV of absorbed energy) are shown as an example in Table 2. To maintain the material balance, the yields must be related through a balance equation such as [42]:

$$G(-H_2O) = 2G(H_2) + G(H^\bullet) + G(e_{aq}^-) = 2G(H_2O_2) + G(OH^\bullet) \quad (1.5)$$

Table 2. Radiochemical yields of products in the radiolysis of pure neutral water at room temperature with hard X-rays, gamma-rays or fast electrons [42].

Species	e_{aq}^-	OH^\bullet	H^\bullet	H_2	H_2O_2	H_3O^+
G-value	2.7	2.7	0.55	0.45	0.71	2.7

Water radiolysis is the starting point for the polymerization mechanism which gives the dosimetric response of polymer gel dosimeters and will be described in the next section.

1.2.2 Polymerization mechanism

Hydrogels used as polymer gel dosimeters consist of an aqueous gel matrix doped with monomers. Monomers are molecules (mostly organic as AAm and Bis) that can react together with other monomers to form a larger polymer chain or three-dimensional network in the process known as polymerization [45]. Polymers are therefore a class of macro-molecules consisting, at least to a first approximation, of a set of regularly repeated chemical units of the same type, or of a very limited number of different types, joined to form a chain molecule whose size can be of the order of 20000 monomers [46].

There are many classes of polymerization reaction mechanisms. In particular, addition polymerization, also known as chain-growth polymerization, occurs with monomers which have at least one double bond (like in a vinyl monomer) [47]. A chain-growth reaction adds new units one at a time to the growing polymer, by rearranging the monomer double or triple bonds [48]. In the process, no molecule is eliminated and no by-product is generated. Such polymerization mechanism takes place in three distinct steps [48]:

1. *Chain initiation*: by means of an initiator (radical or ion) which starts the polymerization process.
2. *Chain propagation*: monomer adds onto the chain and creates a new active site for the next attachment.
3. *Chain termination*: the radical or ion is 'neutralized' stopping the propagation.

When polymerization is initiated by the interaction of high energy radiation, the process is called radiation-induced polymerization. Radiation acts as a catalyst leading to water radiolysis which produces ions and free radicals capable of starting polymerization [49]. The decomposition of water can be summarized as a simplified reaction yielding two reactive radicals (or ions) [34]:



where k_D is the dissociation rate constant proportional to the absorbed dose. These radiolytic products then quickly diffuse outside the radiation track and subsequently react with monomers, such as by binding to an electron of the double bond, and initiate the polymerization [34]:

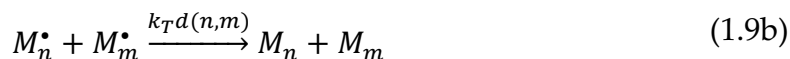


with k_I as the initiation rate constant, the value of which depends on the radical R^\bullet and the species M . The polymerization process continues through chain propagation reactions in which polymeric radicals further react by adding monomers or polymeric groups, increasing the length of the chain or leading to cross-linking [34]:



In Eq. (1.8) a polymer radical with n monomer units reacts with a polymer chain with m monomer units with a propagation rate constant $k_p(n,m)$. The growth of the polymer ends when two radicals react leading to either combination or disproportion [34]:





Primary radicals R^\bullet generated by water radiolysis can also react with growing polymer chains to induce termination or react with dead polymer chains to initiate additional polymerization. In addition to termination reactions, polymeric radicals may also terminate their growth by transferring radical groups to other molecules, such as gelatin polymers [34].

As monomer conversion increases, the gradual formation of large polymeric structures results in the creation of polymer microgels within the aqueous gel matrix which subsequently undergo precipitation bringing about the development of a distinct second phase [50]. The use of crosslinkers, i.e. bifunctional comonomers like the divinyl monomer Bis able to link in two sites, can induce and enhance the microgel formation and precipitation, together with making the polymer chain more rigid [51], [52]. In polymer gel dosimeters in which crosslinking copolymerization occurs giving rise to a copolymer-network (such as AAm/Bis gel system), the polymerization process and its kinetics are affected by the differences in reactivity of the two comonomers and by the change of monomers proportions throughout the reactions [53].

The role of gelatin (or other gelling agent structures such as agarose) during polymerization is mainly to provide a three-dimensional matrix through which the polymers cannot diffuse: when polymers precipitate, they are held in place by the gelatin thus preserving the spatial integrity of the radiation dose distribution [54]. However, it has been shown that gelatin molecules can also act as scavengers of water free radicals, hence the sensitivity of polymeric gel dosimeters is affected also by gelatin concentration [55].

Precipitated polymer microgels are characterized by very high viscosity which essentially reduces the diffusion of the polymeric radicals and therefore also decreases

the efficiency of chain termination by mutual interaction of growing chains (Eq. (1.9)). This change in viscosity has however little effect on initiation and propagation, since it does not affect the diffusion of small monomer molecules. The result is an autoacceleration of the rate of polymerization, which increases with high conversions, known as Trommsdorff-Norrish effect [49].

In Table 3 rate constants for the propagation reaction of various vinyl monomers in aqueous solution with other monomers ($n, m = 1$) are shown.

Table 3. Rate constants in $\text{mol}^{-1} \text{s}^{-1}$ [34].

<i>Monomer</i>	k_p
AAm	$2 \cdot 10^4$
Bis	$6 \cdot 10^6$
Acrylic acid	$1 \cdot 10^3$
MAA	$1 \cdot 10^3$

When oxygen is present in the gel, it interacts with radiolytic products or monomers producing very reactive peroxide radicals [34]:



The creation of peroxide radicals opens an additional mechanism of termination for the growing polymer chain. The peroxide reactions take place at a higher rate than chain propagation reactions causing an effective polymerization inhibition [34]:





This induced termination is the reason why oxygen removal is necessary during fabrication of polymer gel for dosimetry application.

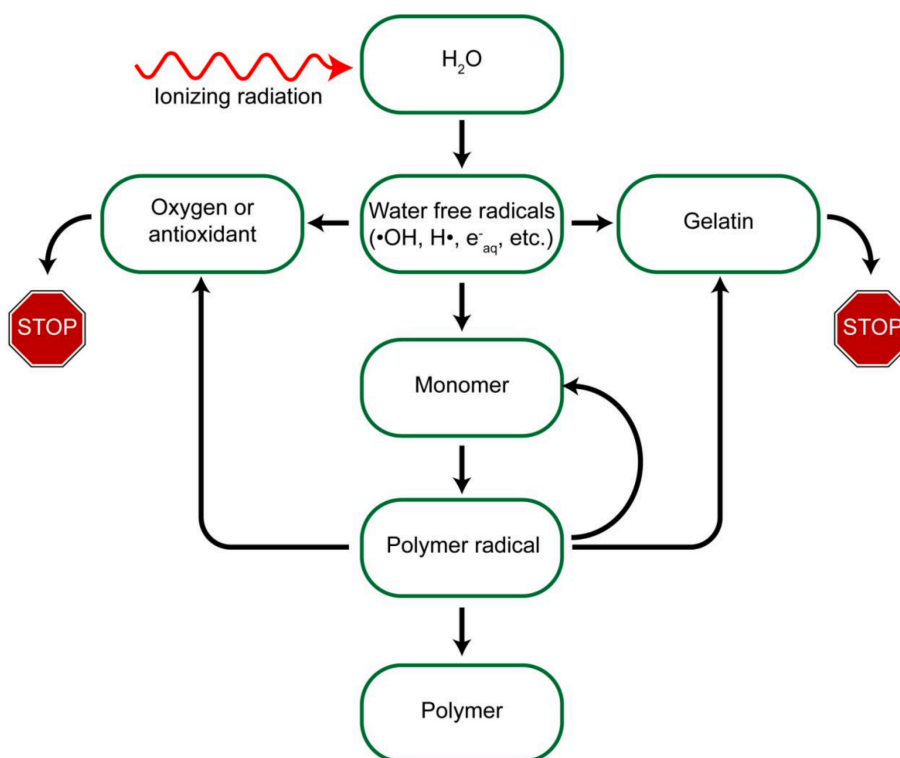
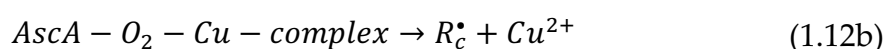
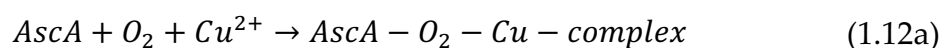


Figure 3. Schematic representation of the interaction between different chemicals in a polymer gel dosimeter during the polymerization process, more specifically for an acrylamide-based dosimeter in a deoxygenated environment [22].

In anoxic dosimeters oxygen inhibition is avoided by working in an oxygen-free environment, such as a glove box, or by expelling oxygen through bubbling nitrogen in the solution during manufacturing. Such procedures greatly increase fabrication time and complexity and at the same time a safe storage and handling of the gels is

required to prevent oxygen infiltration. A significant simplification of the manufacturing process is offered with normoxic dosimeters, in which antioxidants are used to bind and remove free oxygen.

The first normoxic gel formulation (the MAGIC dosimeter) proposed by Fong *et al* made use of ascorbic acid and copper(II)sulphate to scavenge the oxygen. In this system, the oxidation of ascorbic acid is catalyzed by the presence of copper and a copper-ascorbate complex is formed. An oxygen attack on the complex makes the structure unstable and this latter releases the copper ion with the formation of an ascorbate anion radical and a hydroxyperoxide radical [39]. These reactions can be summarized by the equations:



The ascorbate radical complex R_c^\bullet containing the oxygen, among other possible reactions, can undergo termination by reduction of Cu^{2+} successfully disabling the scavenging ability of oxygen:



Although AscA is very effective in MAA-based polymer gel dosimeters, other gel system display either no or very low dose sensitivity using AscA compared to their hypoxic counterparts [56]. Throughout the years, different chemicals have been investigated as oxygen scavenger for polymer gel dosimeters, such as gallic acid, trolox, N-acetyl-cysteine and THPC [39]. Among them, THPC proved to be the most reactive and effective thus becoming the most widely used antioxidant [56]. In the PAGAT formulation, THPC is employed to scavenge oxygen during fabrication.

In the next section, the composition and characteristics of the PAGAT dosimeter will be outlined.

1.2.3 PAGAT dosimeter

As said previously, the PAGAT dosimeter was introduced in 2004 by Venning *et al* by investigating the anoxic PAG formulation combined with the antioxidant THPC. The proposed composition, upon which the gel dosimeters characterized in this thesis are based on, is listed in Table 4.

Table 4. PAGAT formulation. The % refers to weight percentage [40].

Quantity	Species
3%	AAm
3%	Bis
5%	Gelatin
89%	Deionized water
10 mM	THPC

Acrylamide (AAm) is a mono-vinyl monomer with the chemical formula $\text{CH}_2=\text{CHC}(\text{O})\text{NH}_2$ and its structure is shown in Figure 4. The double bond of the vinyl group allows it to undergo addition polymerization and form long, linear chains with no crosslinking [54]. From the physical point of view, it is a white odorless solid, soluble in water and other solvents, while concerning safety it is a dangerous neurotoxin and suspected human carcinogen that requires careful handling [51].

N,N'-methylene-bis-acrylamide (Bis) is a divinyl monomer with chemical formula $\text{CH}_2[\text{NHC}(\text{O})\text{CH}=\text{CH}_2]_2$ and structure shown in Figure 4. It consists of two acrylamides with a methyl radical linking the aminic groups. It is used as a

crosslinking agent due to the presence of two double bonds and is capable of forming several types of links (knots, loops, doublets) [54]. It is an odorless solid and its solubility in hydrogel is limited to approximately 3% in weight relative to the total weight of the gel, even though it can be further increased by addition of co-solvents [57]. Like AAm, also Bis is toxic and therefore its use is associated to potential risks.

Different studies have been performed on PAG dosimeters with different ratios of AAm and Bis, and it was found out that the dose sensitivity is maximum for equal amounts (in weight) of monomer and crosslinker [54].

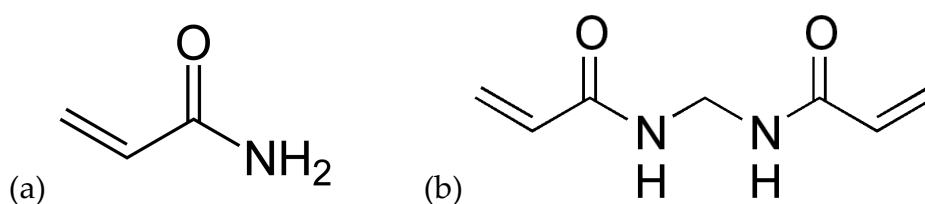
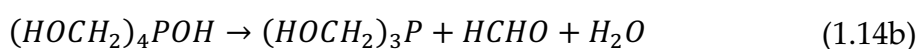
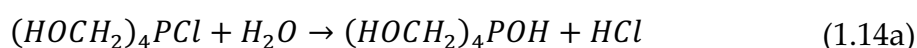
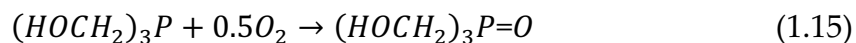


Figure 4. Chemical structure of AAm (a) and of Bis (b).

Tetrakis (hydroxymethyl) posphonium chloride (THPC) is a phosphonium salt with formula $[P(CH_2OH)_4]Cl$. The compound is characterized by phosphorus bonded to four hydroxymethyl radicals to form the cation $P(CH_2OH)_4^+$ and chloride anion Cl^- . Its chemical structure is shown in Figure 5. The scavenging of O_2 by THPC starts with its dissociation in water which creates tetrakis (hydroxymethyl) phosphonium hydroxide (THPOH, Eq. (1.14a)) and subsequently tris (hydroxymethyl) phosphine (THP, Eq. (1.14b)) [58]:



It is THP which scavenges O_2 through the production of tris (hydroxymethyl) phosphine oxide (THPO):



The scavenging of O_2 relies on the fact that the P-CH₂OH linkage is weak and readily cleaved, allowing the formation of a stronger double bond with oxygen [58]. The chemical formula of THPO is given in Figure 5.

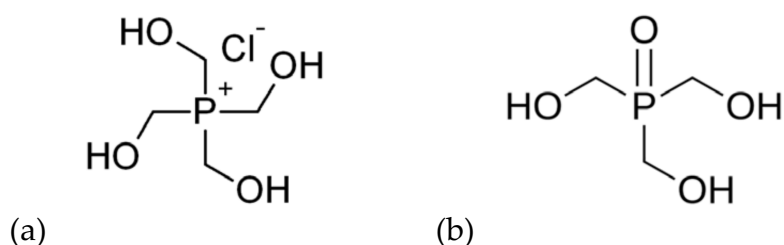


Figure 5. Chemical structure of THPC (a) and of THPO (b).

The amount of THPC was optimized throughout several studies to make the scavenging mechanism more effective and rapid. A concentration around 10 mM of THPC is shown to yield the fastest oxygen sequestration. It is important to use deionized water when manufacturing gel dosimeters as the rate of scavenging of O_2 may be compromised when using tap water due to reactions of THPC with contaminants [58]. These results as shown in the plots in Figure 6. Apart from reducing the influence of oxygen, THPC also leads to a reduced dose sensitivity of the dosimeter and this could be explained by a decreased level of polymerization as the antioxidant itself acts in part as a radical scavenger [59].

Previous studies have also demonstrated the beneficial role of adding polymerization inhibitors, such as nitrobenzene or p-nitrophenol, in the dosimetric composition [60]. These cyclic compounds also act as scavengers by exhibiting high affinity to propagating or initiator radicals and are typically employed to increase shelf

life of stored monomers by preventing premature polymerization or to modify polymeric properties through control of reaction kinetics. The effect of these inhibitors to the gel is to reduce the sensitivity of the dosimeter to extend the linearity range and compensate high-dose saturation of the dose response [60].

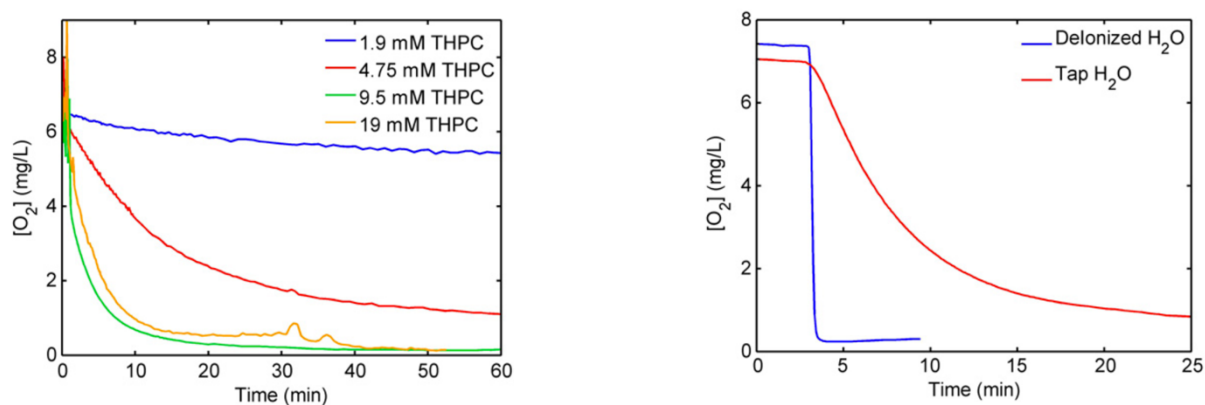


Figure 6. (left) [O₂] versus time for gels with varying amounts of THPC. (right) [O₂] versus time for samples consisting solely of deionized water and tap water [58].

Nowadays the PAGAT formulation presents some issues which are still limiting its use in routine clinical applications. One of them is the lack in reproducibility, partly attributed to temperature effects during manufacturing, irradiation and scanning. It has been shown that between gel manufacturing and irradiation, a significant amount of oxygen can penetrate the vials and alter the response of the gel [52]. The reproducibility issue implies that the gel dosimeter has to be calibrated for each batch, for example by separately irradiating a portion of gel from a batch with a range of known doses [61]. The second criticality is related to the toxicity of acrylamide-based gels, which must be prepared, used and disposed with great care. The use of noxious monomers is a concern among researchers, who are trying to replace them with less harmful chemicals, such as with NIPAM gel dosimeters [62].

1.3 Dosimeter analysis

After fabrication and irradiation, the last step in gel dosimetry involves the scanning of the gel, and through this process the amount of polymerization is quantified to assess the dose response of the dosimeter. Different imaging techniques have been used and optimized for the readout of irradiated gels aiming at acquiring 3D images of the dose distribution to subsequently analyze them. These techniques are based on measuring changes of specific physical properties that occurred in the irradiated dosimeter following polymerization.

Regardless of the specific imaging technique, accurate (both in dose and in space) and precise images should be accomplished as a final result of the dosimetry experiment. The target figure of accuracy in gel dosimetry for high-precision radiotherapy is given by a dosimetric error around 3-5% of the maximum dose in regions of homogeneous dose and a spatial error of about 2-3 mm in regions of high dose gradients [63]. The evaluation of the overall accuracy of the spatial dosimetric distribution obtained with a dosimetric gel is problematic due to the lack of a “golden dosimetric standard”. Dose maps acquired in gel dosimetry are compared with doses obtained by the most reliable dosimetry techniques pertaining a given spatial dimension (ionization chamber, dosimetric film, etc.) [63]. To evaluate the intrinsic dosimetric precision, the concept of dose resolution, written as D_{Δ}^p , is introduced as the minimal detectable dose difference with a given level of confidence, p . The dose resolution is linked to the standard deviation of dose σ_D by the following equation [34]:

$$D_{\Delta}^p = k_p \cdot \sqrt{2} \cdot \sigma_D \quad (1.16)$$

where k_p is a coverage factor for the confidence interval p . For a confidence level of 95%, the dose resolution becomes $D_{\Delta}^{95\%} = 2.77 \cdot \sigma_D$.

Post-irradiation polymerization reactions have been found to continue up for several weeks in irradiated polymer gel dosimeters [61]. For this reason, an appropriate time to image the dosimeter needs to be waited after irradiation, at best so long as changes are slow compared with the imaging time. A minimum of approximately three to four days after irradiation should interpose before imaging is performed [61].

The most common techniques used today for readout of polymer gel dosimeters consist of UV-VIS spectrophotometry, optical-CT, X-ray CT and MRI [34]. The experimental activity conducted during this work made use of spectrophotometric and MRI analysis for the reading of PAGAT dosimeters, hence the working principles and the characteristics of these two techniques will be presented in the following sections.

1.3.1 Spectrophotometric analysis

Spectrophotometry is an optical analysis technique which aims at measuring the absorbing property of the analyte to analyze and quantify its composition. It is widely used in pharmaceutical, chemical, biological industry and research [64]. The absorption measurement is performed by illuminating the sample with monochromatic light and measure its transmitted intensity which is then compared with the intensity of light passing through of a reference sample. For most applications, including gel dosimetry, the range of adopted wavelengths falls between the ultraviolet (UV, $\lambda = 190 \div 350$ nm) and visible light (VIS, $\lambda = 350 \div 800$ nm), hence the technique is referred to as UV-VIS spectrophotometric analysis. In Figure 7, the schematic of a spectrophotometer is shown.

The absorption of incident monochromatic radiation by a sample is governed by the Lambert-Beer law, which predicts an exponential decay of the intensity as the distance travelled by light in matter increases [65]:

$$I = I_0 \cdot \exp(-k[c] \cdot l) \quad (1.17)$$

where I is the transmitted intensity in W/m^2 , I_0 is the incident intensity or the transmitted one through a reference sample in W/m^2 , l is the path length travelled by the radiation in cm and $k[c]$ is a constant in cm^{-1} depending on the analyte concentration c in mol/L .

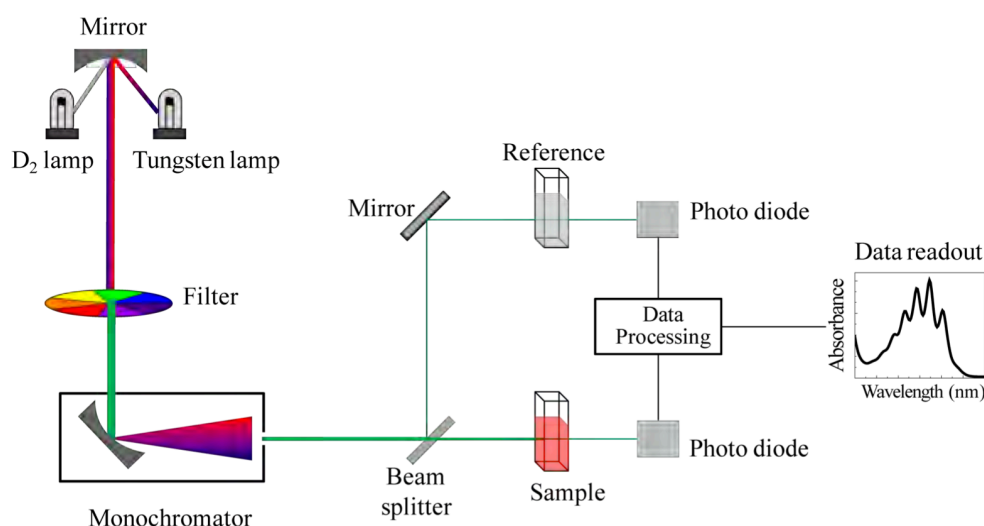


Figure 7. Schematic of a UV-VIS spectrophotometer. The tungsten lamp is used as a source of visible light, while the deuterium lamp produces ultraviolet radiation. The spectrum generated by the lamps is continuous and is later made monochromatic by using a filter and a tunable monochromator [66].

From Eq. (1.17), it is possible to define the absorbance (Abs), which is generally given in decadic terms due to convenience of analytical practice. The constant $k[c]$ is linearly dependent on the concentration c , making Abs in turn directly proportional to the analyte concentration:

$$Abs = \log_{10} \frac{I_0}{I} = \varepsilon_{\lambda} \cdot l \cdot c \quad (1.18)$$

with ε_{λ} being the molar absorption coefficient in $L \cdot mol^{-1} \cdot cm^{-1}$ whose specific value depends on the wavelength λ of the monochromatic radiation. It is important to point out that light absorption measurements can be performed also with samples which do not absorb light but only scatter it. The intensity of the scattered beam at the detector will be attenuated and the measured absorbance will be difference from zero [65].

Optical absorption measurement is a well-established method to determine and quantify radiation induced changes in chemical dosimetry systems. For example, the difference in absorption of light for non-irradiated and irradiated Fricke solutions is exploited to measure the ferric ion concentration produced after exposure to ionizing radiation in Fricke dosimeters. By combining Eq. (1.1) and Eq. (1.18) it is possible to obtain the mathematical relationship which links the dose D to the absorbance Abs :

$$D = \frac{N_a \cdot e}{100\rho \cdot G(Fe^{3+})} \cdot \frac{Abs(D) - Abs(0)}{\varepsilon_{\lambda} \cdot l} \quad (1.19)$$

In Fricke solutions for standard Fricke dosimeters, ferric ions strongly absorb in the UV region at wavelengths near 300 nm, while the addition of xylenol orange as Fe^{3+} ligand in Fricke gels induces the creation of new chemical species with absorption peaks in the visible spectrum at about 580 nm [67]. In general, for radiochromic gel systems, spectrophotometric analysis is characterized by a wavelength interval where the sensitivity is maximum in correspondence of the absorption peaks. The situation is different for polymer gel dosimeters. When spectrophotometry is used to quantify the amount of radiation induced polymerization, no maximum in sensitivity is observed at any wavelength [68]. The reason lies in an increase of light scattering instead of light absorption upon polymerization, which affects all wavelengths as light

is scattered. From the optical point of view, the irradiated polymer dosimeter does not change colour (as it happens for radiochromic systems), but it increases its opaqueness and then it is still possible to linearly correlate the radiation dose to the absorbance at a properly selected wavelength.

The spectrophotometric method offers a relatively simple and cheap analysis and is often a valid alternative to more advanced techniques, such as MRI, which require very complex and expensive instrumentation with limited availability for dosimetry purposes in hospitals [69]. Nevertheless, its main limitation lies in not being an imaging technique which makes the technique unfit to obtain a 3D image of the dose distribution. For this reason, the spectrophotometer is employed for the readout of uniformly irradiated dosimeters in the calibration phase for the assessment of linearity range and sensitivity. A 3D imaging optical analysis can be realized by optical-CT technique. Similarly to spectrophotometry, optical-CT exploits light absorption measurements to quantify the radiation dose in the dosimeter, but the sample is scanned from different directions and the optical projections are combined to create a 3D image of the investigated body.

1.3.2 MRI analysis

Magnetic Resonance Imaging (MRI), developed in 1970s and 1980s, is a diagnostic technique utilized in medical imaging to create pictures of the anatomy and physiological processes of the human body. The images are created using MRI scanners (Figure 8) which are sophisticated and expensive machines where a strong magnetic field is generated in combination with radiofrequency (RF) pulses. The MRI scanner is composed of three major components [63]:

1. *Main magnet*: it produces a homogeneous strong magnetic field B_0 which typically ranges from 0.3 T to 7 T.
2. *Gradient coils*: they create an additional magnetic field, whose magnitude can be varied in space. The resultant total magnetic field is spatially dependent $B(x, y, z)$ and this allows to extract spatial information about the MRI signal.
3. *RF coils*: they are able to generate and/or receive RF waves. Transmit coils produce the RF pulses that excite the nuclei of the scanned object while receive coils capture the RF signal produced by the de-exciting nuclei.

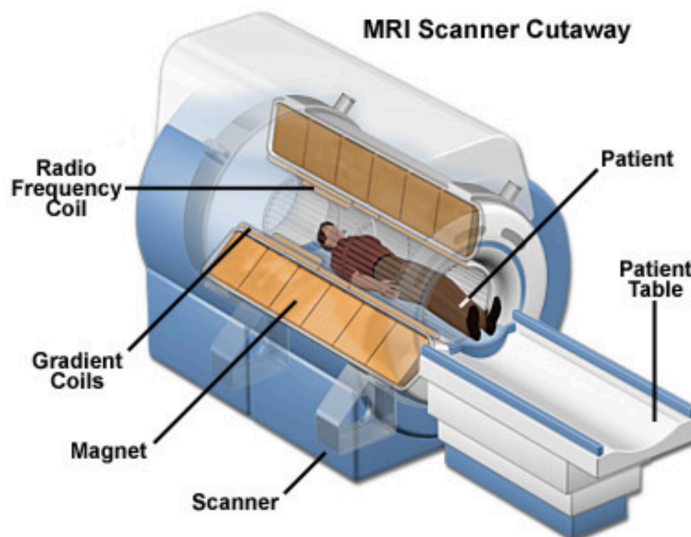


Figure 8. Clinical MRI scanner

The human body, as well as hydrogels, is largely composed of water molecules each of them containing two hydrogen atoms. Hydrogen nuclei, ^1H (protons), possess a non-zero intrinsic angular momentum known as spin which gives them a magnetic dipole moment able to interact with an external magnetic field. During these magnetic interactions, protons can be visualized as magnetic bars with a north and south pole [70]. For a small volume of space containing a large number of protons, it is possible

to define the net magnetization vector \mathbf{M} as the averaged sum of the single magnetic dipole moments per unit volume [71]. In the absence of an external magnetic field, hydrogen nuclei are randomly oriented in different directions and the net magnetization \mathbf{M} in the material is null.

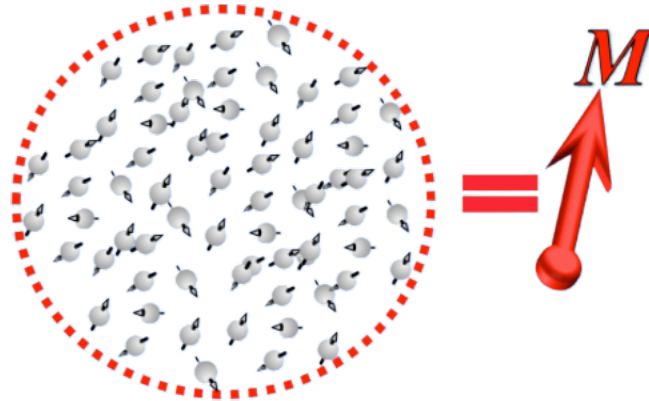


Figure 9. Graphical representation of the net magnetization vector as the averaged sum of the magnetic dipole moments of the single hydrogen nuclei [71].

When the body is placed in a region with strong and static magnetic field (\mathbf{B}_0), the magnetic moments tend to align in the direction of \mathbf{B}_0 but, due to their angular momentum, they start to precess with a given frequency around the field lines like gyroscopes. This phenomenon is called Larmor precession and the related Larmor frequency ω_0 is given by [70]:

$$\omega_0 = \gamma \cdot B_0 \quad (1.20)$$

where ω_0 is in rad s^{-1} , B_0 is in T and γ is the gyromagnetic ratio which, for protons, is equal to $267.54 \cdot 10^6 \text{ rad s}^{-1} \text{ T}^{-1}$ [63]. As can be seen in Eq. (1.20), the Larmor frequency is directly proportional to the magnitude of the external magnetic field. While the single magnetic dipoles precess around the field lines, after a transient their averaged sum results in a net magnetization \mathbf{M} different from zero. At equilibrium, the magnetization vector is aligned in the direction of the main field chosen along z , thus

exhibiting a maximum longitudinal component and a null transverse component perpendicular to \mathbf{B}_0 , that is $M_z = M_0$ and $M_{xy} = 0$.

In order to get a signal from the scanned object, the proton system is excited through a RF pulse, whose magnetic field is perpendicular to \mathbf{B}_0 , which perturbs the net magnetization and brings it out of alignment with the main field. This excitation occurs only if the RF wave has a frequency that corresponds to the Larmor frequency ω_0 , allowing a resonance condition to be achieved. The angle over which the magnetization is flipped towards the transverse plane is dependent on the intensity and length of the RF pulse [63]. After the pulse is removed, the magnetization \mathbf{M} realigns parallel to \mathbf{B}_0 returning to equilibrium through a process named relaxation. During this de-excitation, the hydrogen nuclei dissipate their energy by emitting a measurable RF signal known as free-induction decay (FID) response signal [72]. The frequency of the FID signal is equal to the Larmor frequency ω_0 , hence depending on the magnitude of the main field. It is this signal that is used to obtain an image of the scanned object.

Two types of relaxation can be identified, namely the longitudinal relaxation and the transverse relaxation, which refer respectively to the behaviour of the longitudinal component (M_z) and the transverse components (M_{xy}) of the magnetization vector [70]. The time evolution of $M_z(t)$ and $M_{xy}(t)$ during FID is described by the Bloch equations [71]:

$$M_z(t) = M_0 \cdot (1 - e^{-t/T1}) \quad (1.21a)$$

$$M_{xy}(t) = M_0 \cdot e^{-t/T2} \quad (1.21b)$$

The reestablishment of thermal equilibrium of \mathbf{M} shows an exponential behaviour associated to two time constants, named T1 and T2, usually measured in ms. The first

one, known as longitudinal relaxation time, reflects the regrowth of the longitudinal component, while the second one, called transverse relaxation time, characterizes the decay of the transverse components [71]. The time evolution of $M_z(t)$ and $M_{xy}(t)$ are plotted in Figure 10. From the relaxation times T_1 and T_2 , it is possible to define the corresponding relaxation rates $R_1 = 1/T_1$ and $R_2 = 1/T_2$, which are commonly referred to in gel dosimetry being them proportional to the absorbed dose.

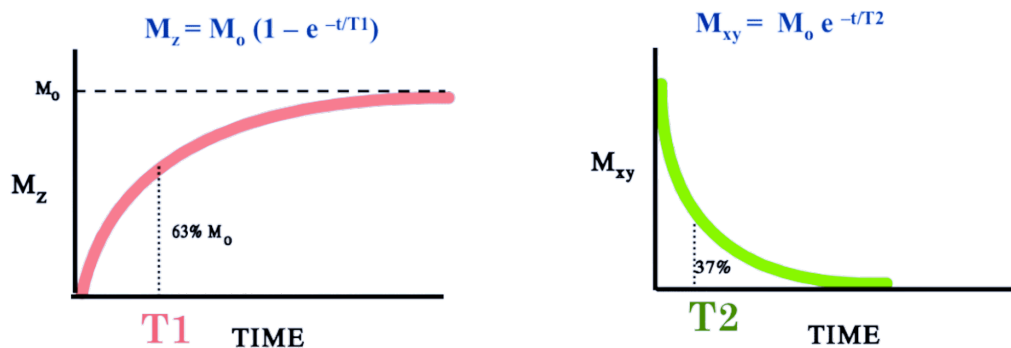


Figure 10. Time evolution of magnetization components during FID [71].

The relaxation phenomenon occurs because the individual spins comprising \mathbf{M} interact with each other and their environment transferring their excess energy. The mechanism of longitudinal relaxation consists in the dissipation of energy to the lattice surrounding the nuclei, therefore it is also known as spin-lattice relaxation and T_1 as spin-lattice relaxation time. In a similar way, the transverse relaxation is also called spin-spin relaxation and T_2 spin-spin relaxation time since the spins dissipate their energy mainly interacting between each other. Although any process causing T_1 relaxation also results in T_2 relaxation, T_2 relaxation may occur even without T_1 relaxation, one of the major causes being the dephasing of the spins due to local field disturbances. For this reason, T_2 relaxation proceeds faster than T_1 relaxation and thus T_1 is always longer than or equal to T_2 [71].

Due to the characteristics of the relaxation mechanisms it is evident that T1 and T2, or equivalently R1 and R2, will possess different values in different points inside the scanned body, depending on the composition and the properties of the material (for example the amount of polymerization). By measuring the values of the relaxation rates throughout the examined object, it is possible to obtain in a non-invasive way three-dimensional detailed images of the object morphology and investigate its functionalities. In Table 5 the approximate values for T1 and T2 in different biological tissues are listed.

Table 5. Approximate values for T1 and T1 at 1.5T in different biological environments [71].

<i>Tissue</i>	T1 [ms]	T2 [ms]
Water	4000	2000
Grey Matter	900	90
Muscle	900	50
Liver	500	40
Fat	250	70
Tendon	400	5
Proteins	250	0.1 – 1.0
Ice	5000	0.001

In an actual MRI measurement, the decay of the transverse magnetization is much faster than what natural atomic or molecular mechanisms would predict. This faster decay is associated to a time constant called T2*, which can be viewed as the observed or effective transverse relaxation time, while T2 can be considered the natural or true decay time of the tissue under examination [71]. T2* is always less or equal to T2, as shown in the graphs of Figure 11. This T2* relaxation comes from an additional spin dephasing caused by main magnetic field inhomogeneities, differences in

magnetic susceptibility among various tissues or materials, chemical shift, and magnetic field gradients applied for spatial encoding [73]. The additional dephasing linked to T_2^* is a reversible effect which can be eliminated by a 180° pulse to obtain what is called a Spin Echo (SE) signal. After the 180° RF pulse, the transverse component of the magnetization will be flipped in the opposite direction (180° flip angle). The spins that were dephasing at a faster rate will rephase and an echo signal will appear from which the true T_2 relaxation can be recovered [63]. The time needed to obtain the SE is named Time to Echo (TE). A graphical representation of the SE process is given in Figure 11.

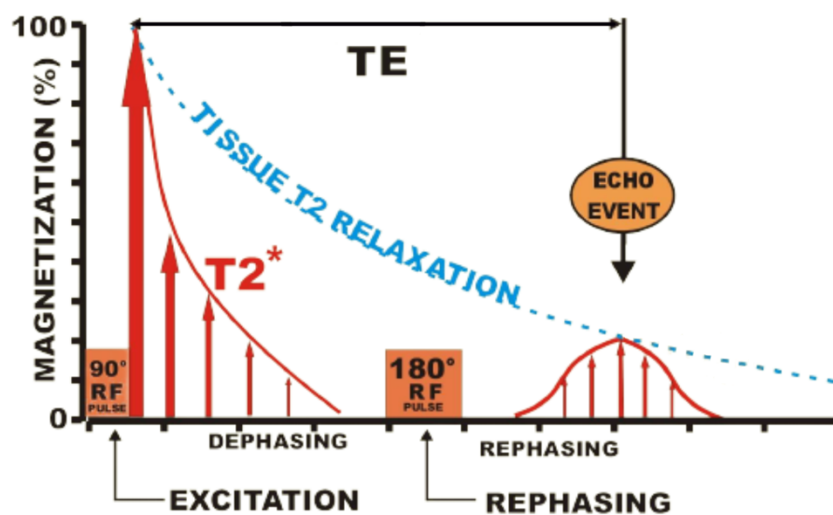


Figure 11. Spin Echo process showing the use of a 180° pulse to rephase the proton spins and produce an echo event for the measurement of T_2 [74].

In order to measure the values of T_1 or T_2 , a sequence of RF pulses is transmitted and the decaying signal from the FID response is collected. The pulse sequences are characterized by a series of TE, for the generation of multiple echo signals, and a repetition time (TR), i.e. amount of time between two successive pulse sequences. By varying the duration of TE and TR in the sequence, it is possible to observe either the T_1 relaxation or the T_2 relaxation. When short TE and TR times are

used, the longitudinal relaxation is measured and T1-weighted images are produced. Conversely, T2-weighted images are produced by using longer TE and TR times.

To extract spatial information from the received MR signal, magnetic field gradients are applied to operate what is known as spatial encoding. By using a space dependent magnetic field $\mathbf{B}(x, y, z)$, the Larmor frequency is made space dependent $\omega_0(x, y, z)$ as can be seen from Eq. (1.20) [63]. The encoding in the axial direction for the slice selection is accomplished by varying the magnetic field along the z direction, while the 2D spatial reconstruction in each axial slice is achieved using frequency and phase encoding gradients. The acquired electromagnetic signals will give a spectrum with different frequencies and phases corresponding with unique spatial positions. These signals are stored in a matrix called k-space and by applying a 2D or 3D Fourier transform the MR images can be retrieved [63].

When it comes to gel dosimetry analysis, MRI was initially proposed as the elected method for the readout of gel dosimeters. In 1984, Gore *et al* [26] showed that MRI relaxation measurements could be used to probe Fricke gel dosimeters. The R1 of an unirradiated Fricke gel dosimeter is small compared to its R2 and for this reason R1 mapping is preferred to R2 one allowing a larger dynamic range of response to be achieved [63]. Similarly to what described for the absorbance in spectrophotometry for Fricke gel analysis, the longitudinal relaxation rate R1 is also proportional to the variation in ferric ions concentration $\Delta[Fe^{3+}]$ and hence, through Eq. (1.1), proportional to the absorbed dose. An equation equivalent to Eq. (1.19) can be written for the dose readout with MRI measurement [25]:

$$D = \frac{N_A \cdot e}{100\rho \cdot G(Fe^{3+})} \cdot \frac{R1(D) - R1(0)}{(r_{eff}^{3+} - r^{2+})} \quad (1.22)$$

with r_{eff}^{3+} and r^{2+} being the relaxivities of, respectively, the ferric and ferrous ion expressed in $L \text{ mol}^{-1} \text{ s}^{-1}$.

For what concerns polymeric systems, the conversion of comonomers to polymer aggregates upon irradiation alters the mobility of the surrounding water molecules which results in a change in R1 and R2. The dose response in terms of R2 for gelatin-based polymer gel dosimeters however is more pronounced, consequently T2-weighted images are usually acquired for the scanning of these devices with the association of R2 relaxation rate to the delivered absorbed dose [63]. To understand the effect of radiation induced polymerization on the magnetic resonance relaxation rate R2, it is possible to consider three different proton pools. These pools are ensembles of protons belonging to molecules that experience the same chemical environment. Three groups of proton pools can be identified in a polymer gel dosimeter [14]:

1. Proton pool of free or quasi-free protons from free water molecules and unreacted monomers. This pool is denoted as mobile (*mob*).
2. Proton pool of growing polyacrylamide network and of water molecules bound to macromolecules (denoted as *poly*).
3. Proton pool of the gelatin matrix and of the water molecules bound to gelatin (denoted as *gela*).

For the R2 measurements performed on polymer gel dosimeters, the relaxation rate of the entire sample is a weighted average of the relaxation rates of the different proton pools [14]:

$$R2 = f_{mob} \cdot R2_{mob} + f_{poly} \cdot R2_{poly} + f_{gela} \cdot R2_{gela} \quad (1.23)$$

where f_{mob} , f_{poly} and f_{gela} are the relative fractions of protons in the respective ensembles. Before irradiation, the second proton pool is empty while the first is at its

maximum. Upon irradiation and subsequent induced polymerization, the second group starts to grow at the expense of the first one. As a result, the relaxation rate will change proportionally to the amount of converted monomers. The mobility of free monomers and of water molecules bound to monomers is relatively high, making the value of $R2_{mob}$ small compared to $R2_{poly}$. After polymerization, the overall molecular mobility is significantly reduced and this leads to an increase of R2 relaxation rate which is put in relation with the absorbed dose [14].

To measure the R2 relaxation rate of a polymer gel dosimeter, a multiple spin echo sequence is commonly employed. The sequence consists of a series of 90° RF pulses followed by a train of 180° pulses to induce a subsequent train of echo signals. The 90° pulses are separated by a repetition time TR, after which the echo train is repeated. Moreover, with a multiple spin-echo sequence, multiple slices can be recorded: after each echo train a new slice is excited with a 90° pulse within the same repetition time [63]. Through this sequence, for the same slice several T2-weighted images (also known as base images) are acquired and the R2 values in each pixel are obtained by fitting an exponential decay curve of the corresponding pixel intensities versus the sequence echo times. The R2 value in a given pixel can be extrapolated from the exponentially decaying pixel intensities of two different T2-weighted images at two subsequent echo times [63]:

$$R2 = \frac{1}{TE_2 - TE_1} \cdot \ln \left(\frac{S(TE_2)}{S(TE_1)} \right) \quad (1.24)$$

where TE_1 and TE_2 are the two subsequent echo times of the two base images and $S(TE_1)$ and $S(TE_2)$ are the pixel intensities at the corresponding times.

A χ^2 -minimization algorithm is usually applied to fit the R2 value from the pixel intensities of the sequence of base images. In this way a so called R2 image can be

generated starting from the base images. Subsequently, through a process of calibration consisting in correlating the radiation dose to the relaxation rate for each pixel of the R2 image, it is possible to obtain a dose map of the irradiated dosimeter. The construction of R2 and dose images using multiple spin-echo sequence is summarized in Figure 12. The sequence should be optimized in terms of TR and number of TE in order to minimize the dose resolution (D_{Δ}^p) and maximize the signal-to-noise ratio (SNR) [75]. Reducing the influence of noise and artifacts in the R2 image considerably contributes to the enhancement of the accuracy in the dose map.

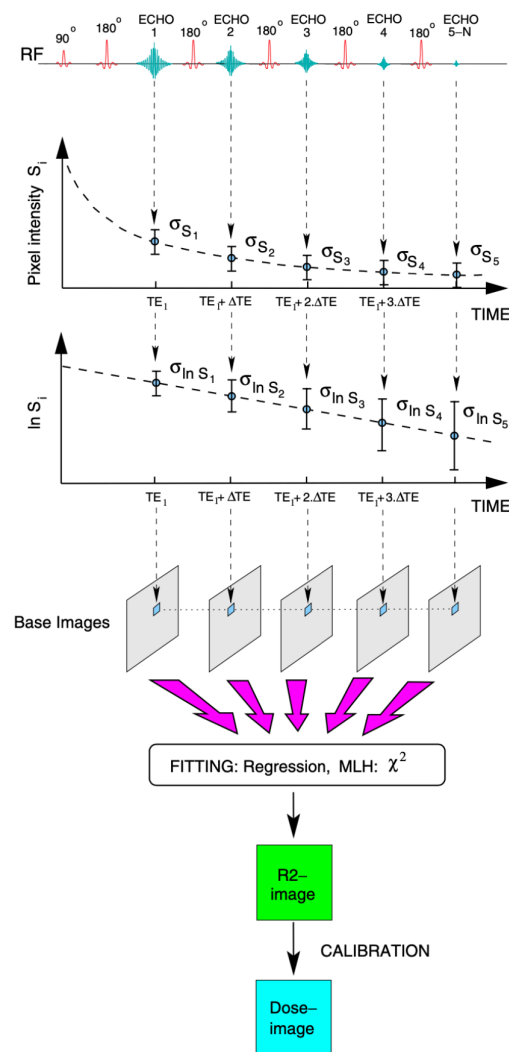


Figure 12. Multiple spin-echo sequence for the acquisition of a dose image with MRI measurement [75].

2. Hadron Therapy

This chapter focuses on the topic of Hadron Therapy (HT), primarily in relation to polymer gel dosimetry. At the beginning, a brief summary of the history of HT will be presented after which the physical principles and characteristics of the technique will be illustrated. Subsequently, attention will be given to the main advantages of the different HT techniques (proton and carbon ion therapy) compared to conventional radiotherapy, both physical and radiobiological.

At the end of the chapter, the subject of HT will be described within the context of polymer gel dosimetry. The problems of high-LET particle quenching and energy dependency of the dosimetric response will be analyzed.

2.1 Introduction

Hadron Therapy, also known as particle therapy, is a general term used to indicate a specific kind of radiotherapy which makes use of accelerated hadrons for the treatment of patients affected by oncological pathologies. The name hadrons collectively refers to non-elementary particles made by quarks and antiquarks including protons, neutrons, pions and ions (which are constituted by nucleons, that are hadrons). It derives from the Greek *ἄδρός* ('hadrós'), which means 'strong', with reference to the strong force through which quarks interact [76].

Currently two types of hadrons are used in clinical practice to treat tumors: protons, ${}^1\text{H}^+$, containing three quarks, and carbon ions, ${}^{12}\text{C}^{6+}$, made of six protons and six neutrons and therefore containing 36 quarks. Other type of light ions, such as helium ions or oxygen ions, together with neutrons in boron neutron capture therapy

(BNCT), are now subject of intense studies to be possibly used in the future [77]. Due to their physical and radiobiological properties, hadrons allow the attainment of a more conformal dose deposition compared to conventional types of radiotherapy with photons or electrons, better sparing healthy tissues located around the tumor and enabling overall a higher control of the disease [78].

Proton therapy (PT) is nowadays an important tool in the clinical practice due to about one hundred PT centres in operation and increasing number of facilities proposed worldwide, while carbon ion radiation therapy (CIRT) with fourteen dedicated centres is showing promising results and is rapidly expanding, even though clinical trials are still needed for the definition of most suitable tumor types and the optimization of protocols [77]. In Table 6, the number of PT and CIRT facilities in operation per country is listed, as reported by the Particle Therapy Co-Operative Group website [79]. Among these, six centres produce both protons and carbon ions and they are thus called multi-particle centres. Four of them are in Europe: CNAO (Italy), HIT (Germany), MIT (Germany) and MedAustron (Austria); one is Japanese (HIBMC) and one Chinese (SPHIC). In addition, 32 proton centres and 5 carbon ion centres are presently under construction (among which one in South America and two in the Middle East), while 28 new PT facilities and 2 CIRT facilities are in the planning stage. About 311,000 patients have been treated worldwide with protons, while about 46,700 patients have been irradiated with carbon ions by the end of 2022 and the numbers are growing year by year [79].

Table 6. Number of PT and CIRT facilities in clinical operation per country to April 2023 [79].

<i>Country</i>	<i>PT facilities</i>	<i>CIRT facilities</i>
EU	22	4
Switzerland	1	-
UK	6	-
USA	44	-
Russia	5	-
Japan	16	7
China	4	2
Taiwan	3	1
South Korea	2	-
Thailand	1	-
India	1	-

The American scientist Robert ‘Bob’ Wilson is regarded as the father of HT for his 1946 seminal paper in which he proposed the therapeutic use of fast protons for the treatment of deep seated tumors on the basis of the physical characteristics of their dose deposition [80]. The first proton therapy treatment took place in 1954 in Berkeley (USA) at the Lawrence Berkeley National Laboratory, using a 184'' cyclotron to irradiate the pituitary gland, while in 1957 the same treatment was successfully repeated in Uppsala (Sweden) with the cyclotron at the Gustaf Werner Institute for Nuclear Chemistry. Undoubtedly, the most impactful facility for the initial development of PT was the Harvard Cyclotron Laboratory located in Boston (USA), where, starting from 1961, radiation oncologists from the Massachusetts General Hospital worked together with Harvard physicists on three clinical studies:

neurosurgery for intracranial lesions (3687 patients), eye tumors (2979 patients) and head-neck tumors (2449 patients) [77]. The results obtained by the Harvard group convinced the scientific community of the superiority of protons compared to X-rays for the treatment of tumors in the proximity of organs at risk. For this reason, PT irradiations started to be carried out around the world in different centres operated at nuclear and sub-nuclear physics laboratories, such as in 1967 at the Joint Institute of Nuclear Research in Dubna (Russia), in 1979 at the National Institute of Radiological Sciences in Chiba (Japan), in 1984 at the Paul Scherrer Institute in Villigen (Switzerland) [77]. It is important to note that, until the end of 1980s, all PT facilities were based on existing accelerators built for fundamental research and adapted to radiotherapy, with all associated drawbacks of sharing human resources and beam time with other activities [76].

A major advancement in particle therapy was achieved in 1990 when the first hospital-based PT facility at the Loma Linda University Medical Center in California (USA) started treating patients. This facility featured a 7-m-diameter 250 MeV synchrotron built by FermiLab and the first rotating gantries designed for PT routine treatment. Soon after, in 1994 at the Heavy Ion Medical Accelerator in Chiba (Japan), the first patient was treated using carbon ions from a 4800 MeV synchrotron. This gap of more than thirty years between the first experimental trials and the first dedicated facilities (much longer compared to X-ray therapy), can easily be attributed to the much larger and much more expensive medical proton accelerators – cyclotrons or synchrotrons – in comparison to electron linacs for X-ray production. However, it is worth mentioning that the high ballistic precision of HT could not be fully exploited until the development of diagnostic techniques able to localize the tumor with sufficient resolution. It was only in the 70s and the 80s, when precise and highly

selective imaging techniques, such as CT, MRI and later PET, became available that the potentiality of HT could be reconsidered for a widespread clinical usage [77].

The layout of a modern HT centre can vary depending on the type of accelerator (cyclotron, synchro-cyclotron or synchrotron), the kind of beam delivery system (passive or active), the use of rotating gantries for the adjustment of the beam angle, the number of treatment rooms, etc. Synchrotron-based accelerator facilities, which is the case of all current CIRT facilities and about one third of PT ones, all feature similar elements [76]:

1. One or more ion sources;
2. An injector linac;
3. A synchrotron accelerator;
4. A high-energy beam transport line. One or more horizontal beamlines and at least one vertical, equipped with instruments that actively “paint” the tumor to achieve the planned dose distribution;
5. In some centres, rotating gantries;
6. Robotic patient positioning devices and in-room imaging verification systems.

As can be seen, a modern HT facility is not only made up of its accelerator, even though it represents a large fraction, about 20-30%, of the construction and operation costs for the overall high-technology multi-room centre [77]. Technological advancements in accelerator science are aiming at reducing the accelerator dimensions, for example by using superconductive magnets in synchrotron rings instead of room-temperature ones to achieve a more compact design [76]. In Figure 13 the layout of the CNAO synchrotron in Pavia (Italy) is shown.

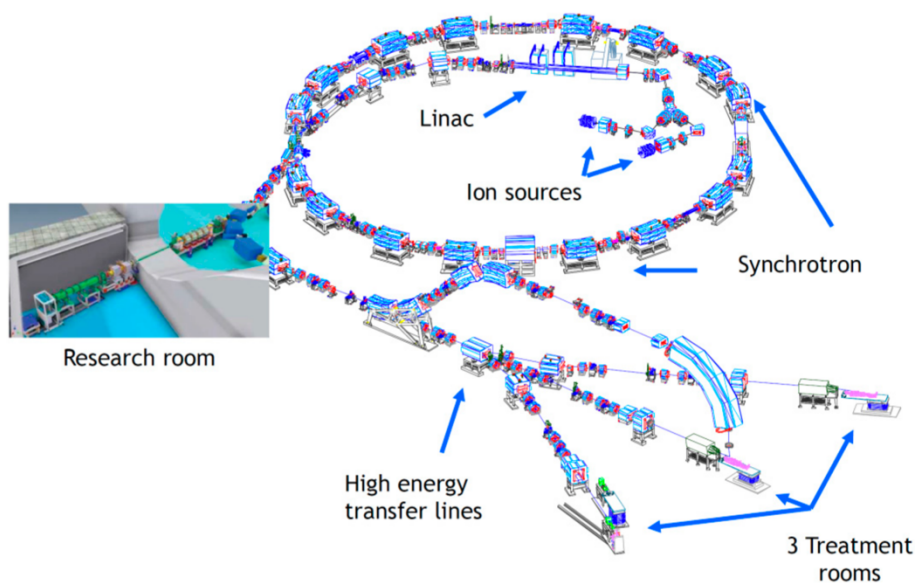


Figure 13. Model of the layout of the CNAO synchrotron. The diameter of the synchrotron is about 25 m [76].

The Italian Ministry of Health has released in 2017 a list of pathologies for which HT treatments are authorized and reimbursed by the National Health Service, while is currently discussing other categories considering the evolution of the technique. The list now contains ten admitted pathologies [76]:

1. Chordomas and chondrosarcomas (of the skull base and of the spine);
2. Meningioma;
3. Brain tumors (trunk);
4. Adenoid cystic carcinomas of salivary glands;
5. Orbit tumors including eye melanoma;
6. Sino-nasal carcinomas;
7. Soft tissue and bone sarcomas (all sites);
8. Recurrent tumors (retreatment);
9. Patients with immunological disorders;
10. Peadiatric solid tumors.

Within these ten categories, it is estimated that every year in Italy around 5000 patients are treated with protons and around 1000 with carbon ions [76].

In spite of the fact that the numbers of patients treated with HT are growing, they are still small compared to all the cases that would benefit from PT or CIRT and are instead treated with conventional techniques. While carbon ions are recommended for particular kinds of radioresistant tumors that represent up to 5% of the total number of oncological patients, protons would be indicated for more than 12-15% of cases treated with X-rays [77].

In the following section, the physical and radiobiological characteristics of protons and carbon ions will be outlined to show their advantages compared to conventional radiotherapy.

2.1.1 Physical properties of Hadrons

A wide variety of interactions takes place when electrically charged hadrons, such as protons and carbon ions, travel through matter dissipating their energy to atoms and molecules of the target material. For what concerns biological tissues, the most relevant interactions are ionizations and excitations of the target atoms, since these processes may lead to changes at the cellular level, most importantly DNA damage, which could resolve into cell inactivation [81].

From the radiation point of view, a beam of electrically charged particles with sufficient kinetic energy is known as a directly ionizing radiation as ionization events occur through the direct and continuous action of the Coulomb force. Compared to electrons, hadrons are heavy particles (the mass of a proton is about 2000 times the mass of an electron) and for this reason the energy transfer takes place essentially through collisional energy losses, while the radiative component (Bremsstrahlung

process) is negligible in the energy range employed in radiotherapy [81]. The mean energy lost by the particle per unit path through ionization and excitation of the target atoms is called the stopping power $-dE/dx$ (keV/ μm) and its mathematical expression is given by the Bethe-Bloch formula, whose relevant dependences are shown in the following equation [81]:

$$-\frac{dE}{dx} \propto NZ \frac{z_p^2}{m_e v_p^2} \left(\ln \frac{2m_e v_p^2}{I(1-\beta^2)} - \beta^2 \right) \quad (2.1)$$

where N (atoms/ cm^3) is the number of target atoms per unit volume, Z is the atomic number of the target atoms, z_p is the atomic number of the projectile ($z_p=1$ for protons or $z_p=6$ for carbon ions), m_e is the mass of the electron, v_p is the speed of the projectile, I is the ionization potential of the target atoms and β is the ratio of the particle speed and the speed of light. The logarithmic term accounts for relativistic corrections and it becomes important only when the projectile speed is sufficiently high to be in the relativistic regime. In the non-relativistic regime, this term can be neglected and the kinetic energy dependence can be emphasized ($E = \frac{1}{2} M_p v_p^2$) making the particle mass M_p appear in the formula. The dependences of the stopping power can be put in evidence considering only the projectile quantities:

$$-\frac{dE}{dx} \propto \frac{z_p^2 M_p}{E} \quad (2.2)$$

The inverse proportionality of the stopping power with respect to the energy has significant consequences in the process of dose deposition: as the particle slows down while travelling in matter, the stopping power keeps increasing up to a point when the energy is not enough to lead to ionization or excitation and other phenomena become relevant before the particle stops [81].

The stopping power is the parameter used to describe the gradual loss of energy of the charged particle as it penetrates into an absorbing medium, however in the evaluation of the radiobiological effects in tissues the concept of Linear Energy Transfer (LET) is commonly considered. The LET (keV/ μm) represents the amount of energy (per unit length) the medium receives from the particle as it travels through it [82]. The difference between LET and stopping power then lies in energy that is radiatively lost to the environment, nevertheless these two quantities are closely related and as a result the LET shows the same dependences of the stopping power reported in Eq. (2.2).

The absorbed dose D (Gy) expresses to the amount of energy deposited per unit mass in matter by the beam and it is therefore directly proportional to the LET of the single particle through the particle fluence Φ (number of particles per unit area) and the mass density of the material by the following equation [83]:

$$D = \frac{\Phi \cdot \text{LET}}{\rho} \quad (2.3)$$

The energy dependence of the LET is then reflected to the absorbed dose D and this defines the depth-dose curve of hadrons in matter: the dose is low when the hadron beam enters the body with particle of high energy, while at the end of the particle range a significant increase in dose is observable as the particles slow down [76]. This peak dose is referred to as the Bragg peak and it characterizes all heavy charged particle depth-dose distributions [81]. This localized deposit of dose in the Bragg Peak region, where severe cell damage is produced sparing traversed and deeper healthy tissue, is one of the main physical advantages of HT providing the technique with an intrinsic high ballistic precision [78]. A comparison of the depth-dose curves between X-rays, protons and carbon ions is given in Figure 14.

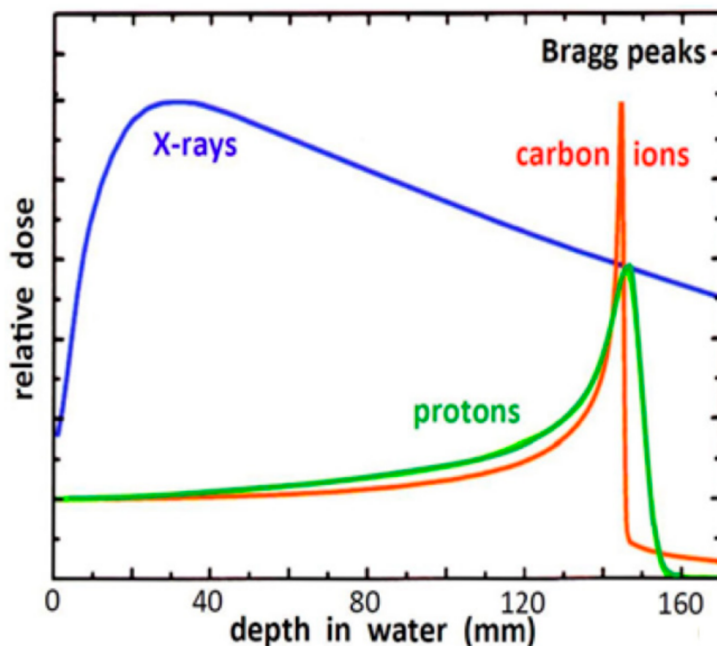


Figure 14. Energy deposition in water by X-ray photons, protons and carbon ions. The energy of the X-rays is 21 MeV, the one of protons is 148 MeV and of carbon ions is 270 MeV/u [76].

It can be noticed that carbon ions produce a Bragg peak that is sharper than the one produced by protons and this is due to the higher charge and mass of the fully stripped carbon ion. This feature implies that CIRT can deliver a dose that is more conformal to the tumor target compared to protons [77]. However, a dose tail in the distal part of the Bragg peak characterizes the depth-dose curve of carbon ions as a result of projectile fragmentation. This fragmentation is caused by inelastic reactions with target nuclei which generate lighter particles with longer range resulting in an extra dose after the main peak [84].

The Bragg peak of a beam of monoenergetic hadrons is relatively narrow (FWHM of 10 mm for protons and 3-4 mm for carbon ions) and to cover the full extension of the tumor in the longitudinal direction a superposition of Bragg peaks with different heights and depths is applied creating a so called Spread Out Bragg Peak (SOBP). The combination of this longitudinal spreading with a displacement in

the transverse direction, either through scattering and absorbing materials (passive system) or through the use of scanning magnets (active system), creates an almost ideal coverage of the tumoral volume with low dose deposited outside the target [76].

Another physical advantage of hadrons for their therapeutic use is provided by the minimal diffusion in the lateral direction associated to Rutherford scattering which leads again to a lower secondary dose to the surroundings of the target [76]. Rutherford scattering, also known as nuclear or Coulomb scattering, is the result of the Coulomb interaction between the projectile particles and the target nuclei during which the total kinetic energy and momentum are conserved (elastic scattering). As a consequence of this interaction, the trajectory of the projectile particle is altered. The differential cross-section for single scattering event in non-relativistic regime is given by [81]:

$$\frac{d\sigma}{d\Omega} \propto \frac{z_p^2 Z^2}{E^2} \cdot \frac{1}{\sin^4 \theta/2} \quad (2.4)$$

with σ being the scattering cross-section in barn, Ω the solid angle in steradian and θ the scattering angle in radian in the centre of mass system.

It is important to note that the overall trajectory of the particles is actually a consequence of a high number of scattering events ruled by Coulomb elastic collisions. This multiple scattering produces numerous deflections and the resulting behaviour is described by the Molière theory, which predicts a beam angular divergence with the following dependences [85]:

$$\Delta\theta \propto z_p/p \quad (2.5)$$

where p is the momentum of the projectile particles, which is proportional to their mass. Since hadrons are much heavier than electrons, they travel a much straighter

path characterized by a small lateral diffusion. In Figure 15, a comparison between the lateral diffusion of protons and helium ions is presented. Helium ions, ${}^4\text{He}^{2+}$, are four times heavier than protons (they are made up of two protons and two neutrons) and have double the charge, therefore at the same velocity their lateral divergence is about half of that of protons. The same is true for carbon ions, twelve times heavier than protons and with six times the charge, and for this reason they show a much sharper lateral penumbra as visible in Figure 16.

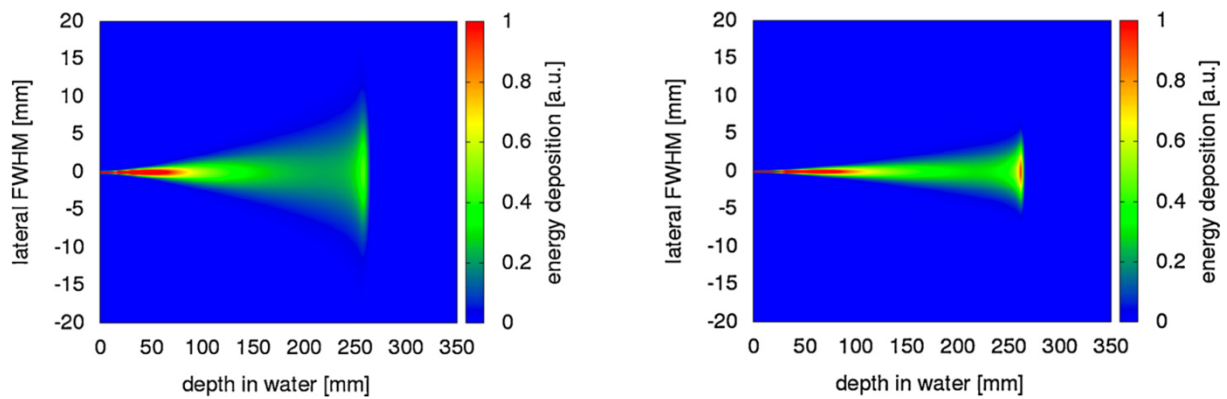


Figure 15. Top view on lateral dimension and energy deposition as function of range for a 200 MeV proton beam (left) and for a 200 MeV/A helium ion beam (right) [86].

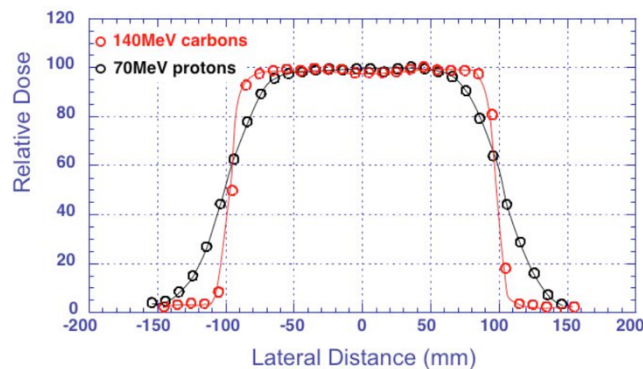


Figure 16. Lateral penumbra of a carbon beam compared to that of a proton beam with a similar range [87].

2.1.2 Radiobiological properties of carbon ions

When it comes to assessing the biological effects of radiation, the absorbed dose D does not properly express the amount of radiation damage at the cellular level and further information and quantities are required to characterize the radiobiological response, such as the type of particles, their energy, their LET and the track structure [88]. As clearly shown by survival curves experiments on irradiated cellular cultures, different types of radiations at the same dose produce very different effects on the cell surviving fraction. Given a fixed incoming particle energy, the type of particles defines the LET and the track structure which ultimately influence the way energy is spatially deposited within the biological tissue: the denser the particle track, as is the case for high-LET particles (protons, α particles, etc.), the greater the energy deposition in a particular micro-target volume, and therefore the more severe damage to biomolecules [88]. The value of the LET also affects the kind of interactions the radiation will have with the cellular system, as at low LET the radiobiological effects are due to indirect actions of reactive radicals that are generated by the radiation and which then interact with the cellular species, while for high-LET values ionizing particles directly break the molecular bonds of cells through direct interactions [89].

An important quantity for the evaluation of the biological effects of radiation is the Relative Biological Effectiveness (RBE), which expresses the different response of cellular cultures to different radiation fields [89]:

$$RBE = \frac{D_{ref}}{D} \quad (2.6)$$

with D being the absorbed dose with the chosen radiation type required to yield a given biological effect on the irradiated tissue, while D_{ref} is the absorbed dose from the reference field producing the same biological endpoint on the same system. The

reference radiation is generally constituted by 250 kV X-rays or Co-60 gamma rays [89]. The RBE is highly variable and it depends on several irradiation parameters and experimental conditions, including the total amount of dose, the dose-rate, the biological effect being analyzed and the kind of cell under irradiation [88]. The general trend of the RBE to the particle LET is shown in Figure 17. Low-LET particles have an RBE equal to 1 since X-rays or gamma photons taken as a reference are associated to low-LET values. The RBE then increases with the LET up to around 140 keV/ μm when it reaches a maximum of about 3. After this value, for higher LET the RBE decreases due to an over-killing effect which occurs when the track is so dense that the energy depositions are concentrated to a lower number of cells [89].

As visible in the plot of Figure 17, the RBE of protons is on average equal to 1.1, therefore leading to only a slightly higher biological effectiveness than photons or electrons. In fact, the main advantage of PT lies in a superior ballistic precision compared to conventional radiotherapy. Conversely, the biological effectiveness of carbon ions can be three times higher than protons as an average RBE equal to 3 can be obtained making CIRT more effective in treating radioresistant tumors, which represent about 5% of the cancers irradiated with X-rays every year [77].

Another radiobiological advantage of carbon ions over protons is related to the oxygen effect and is quantified by a low Oxygen Enhancement Ratio (OER). The radiosensitivity of a biological tissue is strongly affected by its oxygen content, as the presence of O_2 during irradiation leads to the formation of very reactive superoxide radicals (see Section 1.2.2) which react with the cellular system through indirect interactions enhancing the biological response. For this reason, hypoxic areas of tumors (with O_2 partial pressures ≤ 2.5 mmHg), which arise due to imbalance between supply and consumption of oxygen, are particularly difficult to be treated leading to hypoxia-induced radioresistance [90].

Similarly to the RBE, the OER is defined as ratio of doses required to achieve the same biological effect under hypoxic and normoxic conditions [90]:

$$OER = \frac{D}{D_0} \quad (2.7)$$

where D is the absorbed dose that induces a given biological effect to the tissue at its real oxygen concentration and D_0 is the dose which would be required for the same effect if the tissue were completely oxygenated [89]. The OER shows dependences on many factors as analogously described for the RBE and its general trend to the particle LET is given in Figure 17.

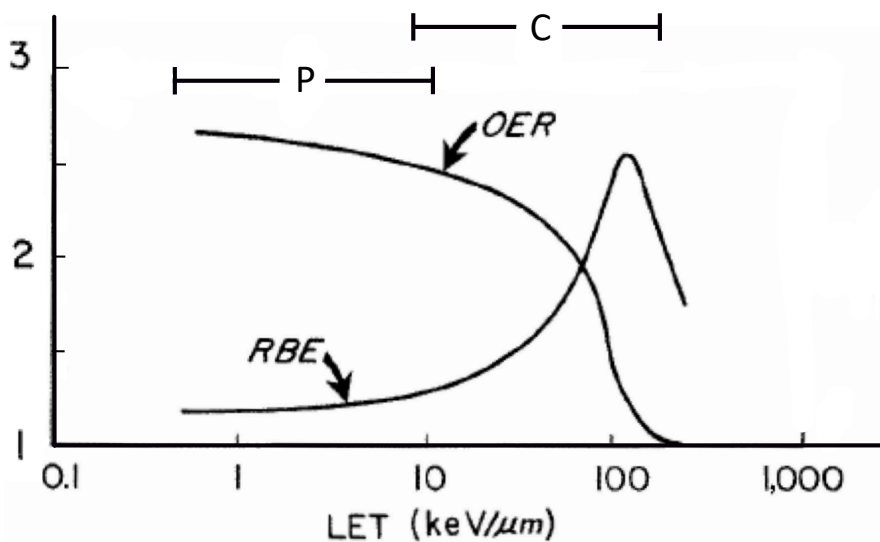


Figure 17. RBE and OER vs LET: as LET increases, RBE reaches a maximum around 100 keV/μm before it trends back down; OER decreases with LET until it reaches 1 at around 100 keV/μm. Typical LET ranges for protons (P) and carbon ions (C) are also shown [89].

Low-LET particles are characterized by an average OER around 2-3, meaning that two or three times the same amount of dose needs to be delivered to yield the same effect with respect to a corresponding well-oxygenated tissue, this leading to possible complications to the healthy surrounding areas. As the LET increases, the OER decreases reaching an average value of 1 around 100 keV/μm, indicating that the

presence of oxygen is no longer relevant at high LET as the biological effects are carried out mainly by direct interactions without any contribution from radicals. Compared to protons, the oxygen concentration of the tumor is less critical for CIRT due to an OER close to 1.

In summary, HT using high-LET particles (like carbon ions) shows important clinical advantages from the radiobiological point of view which can be very effective in the treatment of radioresistant hypoxic tumors due to and higher RBE and a reduced dependence on oxygen content [90]. A more effective treatment requiring the delivery of a lower dose is beneficial also in protecting healthy normal tissues from further complications.

2.2 Gel dosimetry in Hadron Therapy

The unique characteristics of charged hadron beams outlined in the previous section, specifically the sharp delivery of dose in correspondence of the Bragg peak where severe damages are localized while sparing healthy tissues, have increased the interest in direct 3D dose verification methods [34]. The extreme conformity of the dose distribution makes HT more technically demanding for what concerns dosimetry verification as any geometrical uncertainty or setup error can seriously compromise the efficacy of the treatment. For example, the possibility of depositing significantly too much or no dose at all in a given volume due to uncertainty on the particle range can result in either serious damage to healthy tissues or treatment failure due to lack of tumor control [91]. In order to achieve highly precise and accurate treatments, careful characterization of particle beams is then required and this is presently performed by using ionization chambers or film dosimeters [92].

Gel dosimetry has the potential to be an accurate and versatile method for the verification of three-dimensional dose distributions with capabilities which are beyond the currently available dosimetry systems, in term of spatial resolution and radiological tissue equivalence [93]. Since gel dosimeters have been introduced, their radiological characteristics in the irradiation with photons and electrons from conventional linacs have been well investigated. On the other hand, up to now few studies have been reported regarding the irradiation of gel dosimeters with high-LET particle beams employed in HT and only sparse data are available addressing the influence of LET on the gel dose response [94]. In these studies, good agreements have been observed both experimentally and with simulations in terms of geometrical information since no significant image distortions or artifacts of the dose distributions were found [95], [96]. The possibility to record with sufficient accuracy particle range or beam dimension makes gel dosimeters suitable for qualitative and non-absolute dosimetry in HT [97]. In spite of these good geometrical agreements, when it comes to quantitative dosimetry, for all kind of gel dosimeters (both radiochromic and polymeric) a strong suppression in dose response at depths near the Bragg peak is observed due to a decrease in sensitivity [91]. In Figure 18, the depth-dose curves of protons (left) and carbon ions (right) measured using polymer gel dosimeters are reported: a good correspondence in terms of depth of the peaks is visible, alongside an evident suppression of the Bragg maxima (especially for carbon ions).

A signal reduction at the Bragg peak is common to most solid-state detectors and for gel dosimeters. The cause can be split into two contributions: a saturation effect can occur when the linearity range of the detector is overcome, given that the physical dose at the peak is large; a second effect can also be identified in a purely quenching phenomenon associated to an LET-dependence of the detector sensitivity [91]. The two dose-signal curves in Figure 19 are measured at different positions (that is at fixed LET,

as the LET changes with depth) and their difference highlights the presence of a quenching effect.

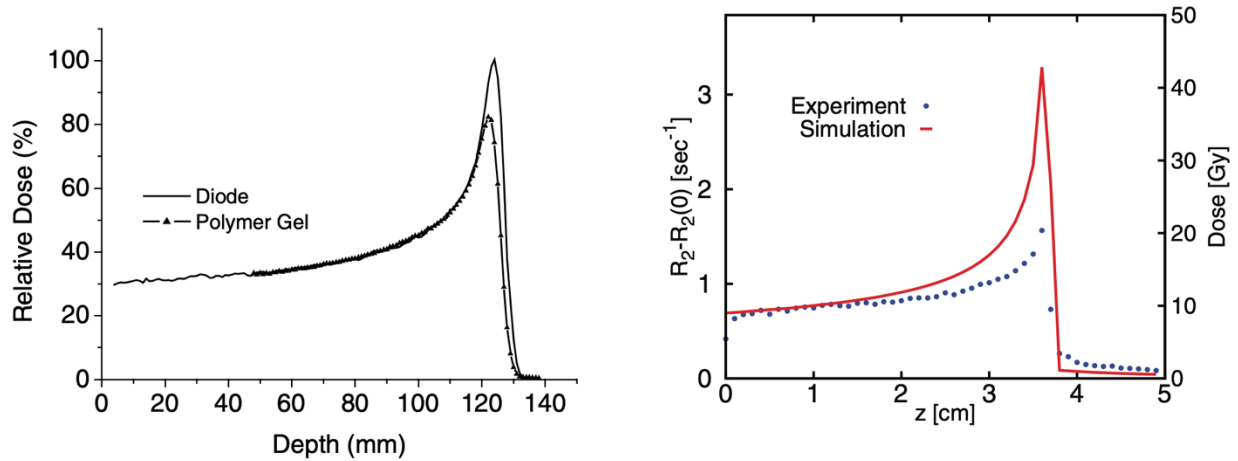


Figure 18. (left) Relative depth dose curve for monoenergetic 133 MeV proton beam measured using MAGAT polymer gel dosimeter and silicon diode detector [98]. (right) Comparison between the measured depth-signal curve in PAGAT polymer gel dosimeter and the MC calculated depth-dose curve for 135 MeV/u carbon ion beam [99].

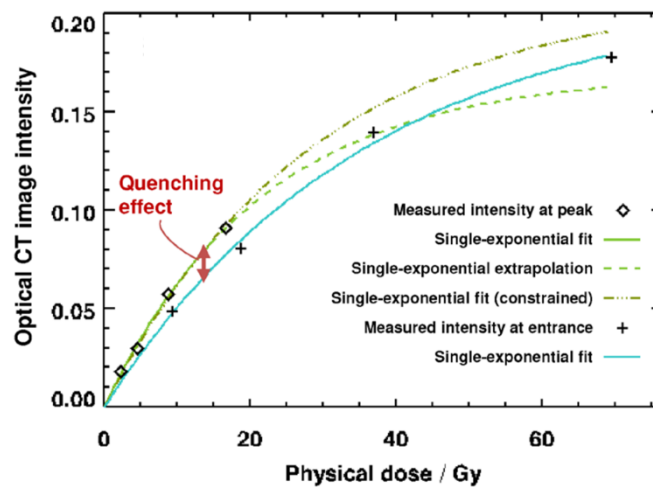


Figure 19. Dose-signal curves measured at peak and entrance regions using PRESAGE (radiochromic) gel dosimeter irradiated with 60 MeV proton beam [91].

These results indicate that the strong suppression at the Bragg peak due to quenching effect is linked to the increase in LET in the last part of the particle track, where the energy of the particles is low, making the dose sensitivity of the dosimeter depth-dependent. The analysis performed on a MAGAT dosimeter irradiated with a 133 MeV

monoenergetic proton beam is reported in Figure 20 as an explicative example. The LET values plotted as a function of depth are calculated using MC method, the range obtained being approximately between 1 to 12 keV/ μm . In the same graph, the relative sensitivity S_{rel} of the gel is also shown as a function of depth (and hence of the LET). The values of S_{rel} are calculated as the ratio of the relative dose measured using the gel and the relative dose of a silicon diode detector at different depths ($S_{rel} = D_{gel}/D_{diode}$). In agreement with previous experiments using low-LET particles, no significant quenching effects are observed for depths at which the LET < 4.9 keV/ μm , where S_{rel} is close to one, confirming that the dose response is not altered at LET values typical for photons and electrons in the clinical energy range. For larger depths at the end of the Bragg peak, S_{rel} decreases drastically reaching a minimum of 0.3 [98].

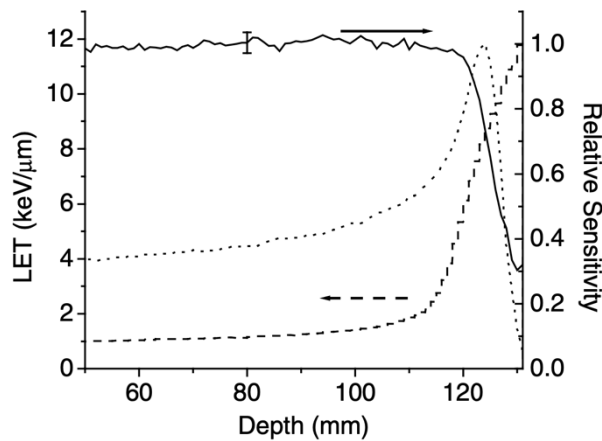


Figure 20. The variation in LET as a function of depth for a monoenergetic proton beam (dashed curve, left-hand scale) and the measured relative sensitivity for the gel dosimeter (full curve, right-hand scale). Also shown is the depth–dose curve for the proton beam (dotted curve), normalized to 100% at the Bragg peak [98].

The decrease in dose response due to LET effects at the Bragg peak does not have a clear and unique physical interpretation. On one hand, it may be attributed to a larger free radical recombination occurring at high LET which decreases the amount of polymerization reaction. As the LET increases, the interaction sites created by the radiation in the gel are close together and the ion clusters overlap facilitating

interradical recombination. The yields of free radical from water radiolysis, such as H^\bullet , OH^\bullet and e_{aq}^- , are known to decrease with increasing LET and this consequently leads to a reduction of polymerization and a decrease in dose sensitivity [98]. Alternatively, a larger density of polymer chains at high-LET values might promote a faster termination of the polymerization reactions resulting in a lower signal at Bragg peak: as the kinetic energy of the particles lowers (and the LET increases), the distance between polymer chains along the particle track reduces, the termination rate increases and the dose response is thus suppressed [100]. Both these explanations can be visualized within the phenomenological framework of the diffusion kinetic spur model. A spur is defined as a localized microscopic area along the particle track involving several water radicals and it propagates inside the medium like a diffusion of elementary wave. As the distance of successive spurs reduces while the kinetic energy of the particle decreases, the density of spurs on the particle trajectory increases with the LET entailing a response suppression [100]. Figure 21 is helpful to picture the phenomenological behaviour.

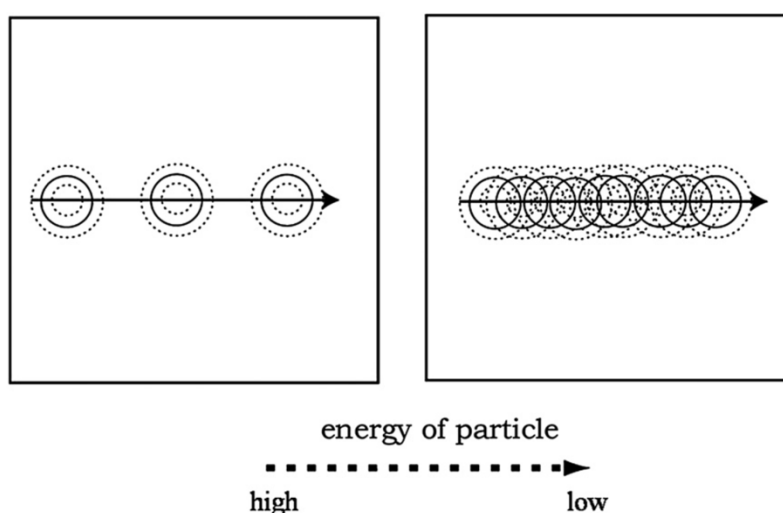


Figure 21. Illustration of the spur model to clarify the energy (LET) dependence of the dose response. The solid arrow represents the single particle track, while the solid and dotted circles visualize the propagation of the spurs [100].

Regardless of the interpretation or the empirical model applied, the issue of LET-dependence does not readily allow the use of gel dosimeters for 3D absolute hadron dosimetry. For an implementation of gel dosimetry for field verification and quality assurance in HT, the LET effects need to be compensated [96]. Two possible strategies can be considered to overcome the problem of dose suppression at high LET. The first involves establishing an LET calibration response curve specific for the hadron particle and gel dosimeter. The construction of this curve is a challenging task, given the high dose gradients in the particle depth-dose curve and the complexity of multiple beams settings [92]. The second possibility implies the use of less sensitive gel formulations to minimize saturation and quenching effects. The sensitivity of PAGAT dosimeters can be easily tuned adding inhibitors like p-nitrophenol to the initial composition. This solution has limitations, especially for what concerns measuring low dose regions [92].

At present, without a compensation for LET effects, the dependence of the sensitivity leading to a dose under-response does not allow an absolute dose measurement for HT gel dosimetry and hence more studies are necessary.

3. Materials and methods

In this chapter, an overview of the procedures followed for the PAGAT dosimeter preparation will be provided, together with a description of the irradiation setup implemented at the CNAO synchrotron accelerator. The optical and MRI methods employed for the dosimeters analysis and subsequent data processing will be discussed specifying the parameters of the adopted instrumentation.

3.1 Gel preparation

The gel preparation for the PAGAT gel dosimeters was conducted following specific procedures, with the composition details provided in Table 4 of section 1.2.3, obtained from the literature [40]. To extend the linearity range of the gel, an additional 2.5 ppm of p-nitrophenol was incorporated as inhibitor, as suggested by previous studies [60]. Table 7 summarizes the gel composition and role of each species used for the gels prepared in this thesis work.

Table 7. PAGAT gel composition as used during the analysis. The % refers to weight percentage.

Species	Role	Quantity
AAm	Monomer	3%
Bis	Cross-linker	3%
Gelatin	Gelling agent	5%
Deionized water	Solvent	89%
THPC	Oxygen scavenger	10 mM
p-nitrophenol	Inhibitor	2.5 ppm

The preparation begins by adding AAm and Bis to 55% of the final deionized water volume. The solution is then heated to 50 °C using a hotplate and stirred with a magnetic stirrer until the monomer and cross-linker are completely dissolved, resulting in a limpid solution. Heating and stirring are necessary to induce a quicker monomer dissolution as Bis at 3% concentration is near its solubility limit in water. In the meantime, in a separate container, porcine skin gelatin is added to the remaining 45% water volume. This solution is also heated to 50 °C and stirred for a minimum of 15 minutes until complete dissolution is achieved. Once both solutions were limpid, they are allowed to cool down to 30°C before being mixed together. Cooling prior to mixing is needed to prevent heat-induced polymerization of the monomers. Water lost through evaporation during the heating process could be reintegrated after the solutions combination. Once the two solutions are sufficiently mixed, the appropriate volumes of p-nitrophenol and THPC are added drop-wise using volumetric pipettes while stirring to guarantee a uniform distribution of these components.

Depending on their intended use, the dosimetric solutions were poured into different containers. Samples for calibration and stability assessment were placed in PMMA spectrophotometric vials of 5 mL, which were then sealed and wrapped using Parafilm. Phantoms for volumetric dose mapping were prepared in HDPE hollow cylinders of 0.5 L, provided with screw tops. The different containers are shown in Figure 22 and Figure 23. After preparation, the samples were stored in a refrigerator at approximately 7 °C to allow the gelatin to solidify and irradiation was performed at least after 12 hours to ensure stabilization of the dosimetric composition. To avoid gelatin liquefaction, the dosimeters were kept refrigerated at all times possible.

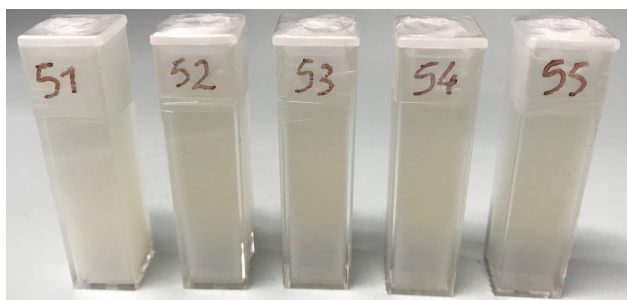


Figure 22. Set of spectrophotometric cuvettes containing PAGAT gel composition. External dimensions: 11 x 11 x 50 mm.



Figure 23. Volumetric cylindrical phantom containing PAGAT gel composition next to three spectrophotometric cuvettes as comparison. External phantom dimensions: 75 mm base diameter, 134 mm height to the shoulder, 57 mm lid diameter, 165 mm total height.

3.2 Irradiation

The irradiation of the gel dosimeters was conducted using monoenergetic proton and carbon ion beams generated by the 25-metre diameter synchrotron accelerator at CNAO (Centro Nazionale di Adroterapia Oncologica) facility in Pavia (Italy). The synchrotron extraction energy ranges from a minimum of 60 MeV for protons up to a maximum of 400 MeV/u (4800 MeV) for carbon ions [101]. Before the irradiation of the

samples, the machine outputs were carefully characterized in terms of megaparticles per Gy to ensure the accurate delivery of the desired dose. The megaparticle is a unit that in HT is analogous to the Monitor Unit (MU) applied for Linacs delivery control. This characterization was accomplished using a Farmer ionization chamber.

To mitigate any buildup effect and guarantee tissue equivalence, a support structure consisting of several layers of water-equivalent RW3 was employed [102]. This configuration, visible in Figure 24, involved overlapping the layers, with the middle one acting as a frame to accommodate the cuvettes (Figure 24 (right)). The upper layer of RW3 was such that the centres of the cuvettes were at a depth of 20 mm, where the effective measurement point was assumed to be. The use of this support structure helped maintain consistency during irradiation and avoid any distortions caused by the interface of the dosimeters with the surrounding.

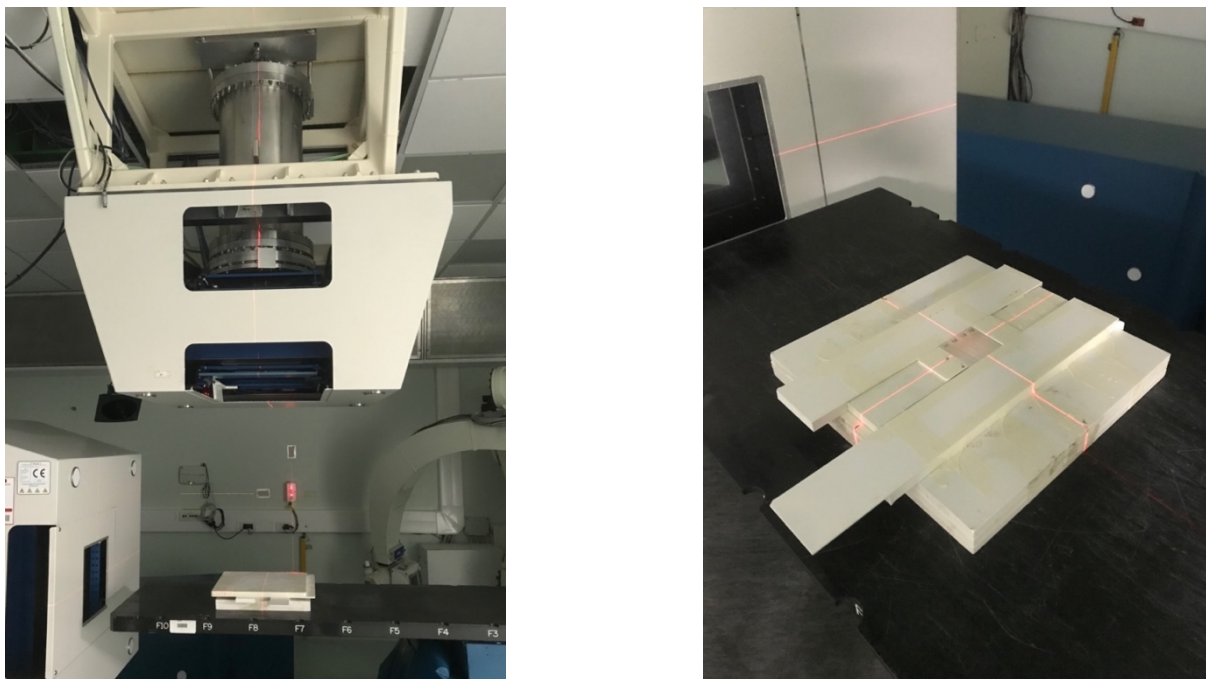


Figure 24. (left) Irradiation set-up for the cuvettes using the vertical beamline. (right) RW3 layer support for the uniform dose irradiation of a group of four cuvettes.

All irradiations were carried out using the vertical beamline of the second treatment room of CNAO. A highly accurate robotic patient positioning system with laser trackers guaranteed to maintain the same delivery position between successive irradiations [103].

The cuvettes were positioned horizontally in groups of four, as illustrated in Figure 24 (left). The beam was spread out laterally using an active paint modality, covering an area of 7.2 x 7.2 cm. The energies of the beam were carefully selected to keep the samples at the depth-dose profile plateau, ensuring a uniform dose distribution across the four samples and minimizing any dose gradients in the longitudinal direction. This allowed to have groups of four samples uniformly irradiated at the same dose to perform the statistical analysis. The irradiation scheme for the cuvettes was structured as follows: doses of 1 Gy, 2 Gy and 4 Gy using monoenergetic protons of 97.54 MeV (corresponding to a Bragg peak at 70 mm depth in water) and 174.87 MeV (201 mm); same doses using monoenergetic carbon ions of 181.17 MeV/u (70 mm). Since the position of the Bragg peak in water uniquely depends on the energy of the particles, it is common in HT to refer to a monoenergetic beam in terms on depth (in mm), being the extension of the dose distribution a much more relevant parameter for the clinical usage than the energy of the particles.

For the acquisition of the volumetric response, the phantoms were positioned vertically and irradiated from the bottom using single-spot beams at various energies. RW3 plates were not required since the overall dose profile develops inside the phantom itself. This approach enabled the recording of three-dimensional dose distributions along different depths within the gel dosimeters. In total, three phantoms were irradiated: two using monoenergetic protons at energies corresponding to 70 mm (97.54 MeV) and 101 mm (118.20 MeV), and one using a monoenergetic carbon ion beam of 90 mm (208.58 MeV/u) energy.

3.3 Dosimeter analysis

The gel dosimeter analysis consisted in optical and MRI readouts carried out at various time intervals after irradiation to assess the temporal stability of the dose response. Spectrophotometry and MRI scanning were employed to analyze the cuvettes, while MRI only was used for the volumetric phantoms. The initial measurements were performed at least two days after irradiation to allow the polymerization response to develop.

3.3.1 Spectrophotometric analysis

Optical analysis of the cuvettes was performed by utilizing a LAMBDA 650 UV/Vis spectrophotometer (PerkinElmer [104]). A sampling wavelength of 550 nm was selected, with a scanning time of 0.2 s. An additional cuvette containing deionized water served as the absorbance reference throughout the reading, as shown below in Figure 25 (right).

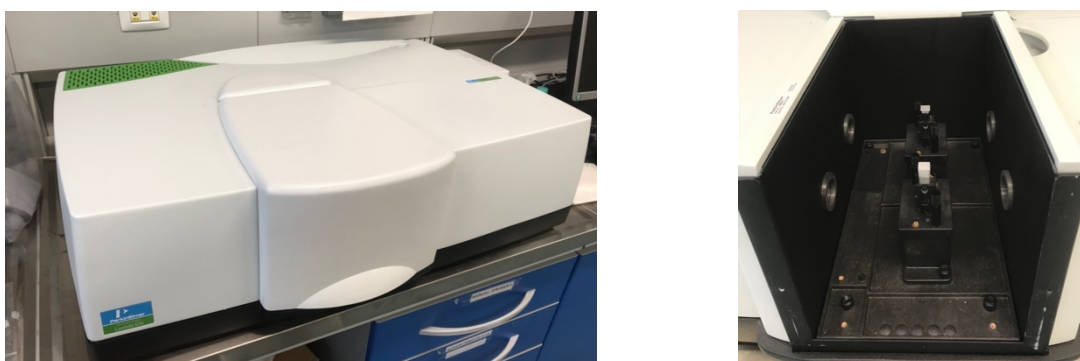


Figure 25. (left) LAMBDA 650 UV/Vis spectrophotometer; (right) sample and reference holders inside the instrument.

As stated in section 1.3.1, polymer gel dosimeters do not show any optical absorbance peak, therefore the sampling wavelength of 550 nm was selected in accordance with previous studies based on the PAGAT optical absorbance spectra.

The goal of this analysis was to construct dose-absorbance curves to characterize the polymerization response in terms of sensitivity and linearity range. In order to do so, the mean absorbance of the blank specimens was subtracted from the one of the irradiated samples and a linear interpolation with the dose values was performed. Temporal stability was evaluated by repeating the measurements over a two-month period following irradiation.

3.3.2 MRI analysis

Magnetic resonance analysis was performed using clinical MRI scanner available at the CNAO facility, a 3 T Magnetom Skyra Fit (Siemens [105]). As mentioned before, for the volumetric phantoms the analysis was done only by MRI in order to suitably capture their three-dimensional dose information, while the cuvettes response was characterized with MRI as an additional method to the optical technique. The measuring setup for the phantoms is shown in Figure 26.



Figure 26. Phantom in the automatized bed for MRI scanning.

For all dosimeters, a multi-slice multi-echo pulse sequence was adopted in order to produce T2-weighted images which were then elaborated into R2 maps. The scanning echo train consisted of 32 TE values ranging from 20 to 640 ms, with

increments of 20 ms. The dimensions of the voxel measured 1.4 x 1.4 x 1.4 mm. The samples were positioned on an automatized bed and the whole acquisition took approximately one hour.

The MRI raw data consists of several T2-weighted images recording the signal intensity at different echo times. In particular, for the chosen sequence, a total of 32 images (one for each TE) were acquired per slice, each pixel value capturing the signal intensity as it decays exponentially in time according to different R2 relaxation rates (Figure 27). To enhance the signal quality, each T2-weighted image underwent six repeated acquisitions, which were then automatically averaged by the MRI software. To generate R2 maps of the gels starting from the MRI raw data, an image reconstruction algorithm previously developed in the Matlab environment was adapted. The algorithm encompasses several steps, as outlined below:

1. Application of a mask to the MRI images to select exclusively the signal originating from the sample and filtering out the empty (air) space surrounding it. This step is important to reduce the Matlab computational time and obtain a cleaner sample image.
2. Fitting of the signal intensity pixel-by-pixel in the T2-weighted images using a maximum-likelihood estimation approach with χ^2 minimization, as suggested in the literature [106]. Through this fitting process, the R2 relaxation rates are calculated based on the signal decay in time according to the appropriate Bloch formula (Eq. (1.21b)).
3. Construction of R2 maps where the relaxation rates obtained from the fitting algorithm are assigned to each pixel in the T2-weighted images.
4. Extraction of the mean R2 value from a region of interest in the R2 map, enabling characterization and calibration. Calibration allows the construction of absorbed dose maps of the sample by the creation of R2-dose curves.

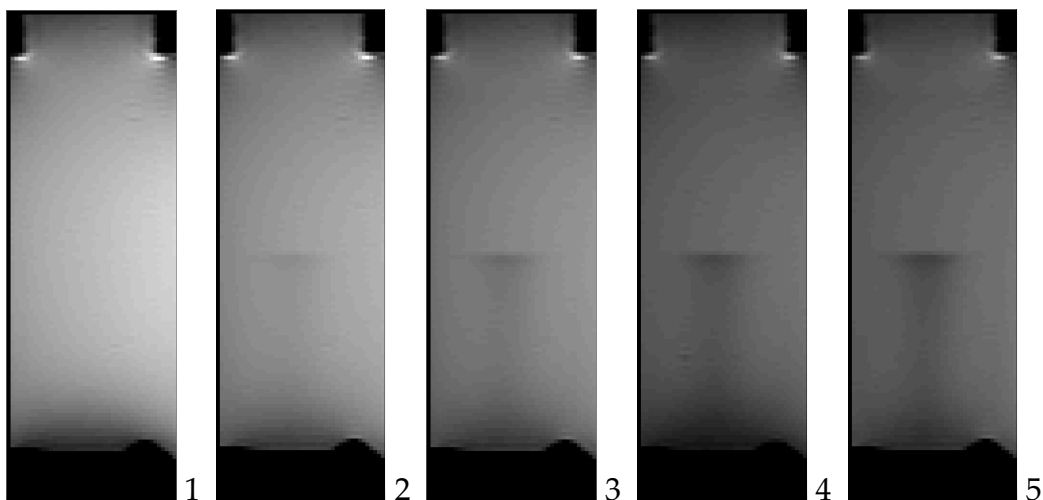


Figure 27. Five T2-weighted images at different TE times of the phantom irradiated with protons at 70 mm. From 1 to 5, the TE are equal to: 20 ms, 180 ms, 320 ms, 520 ms and 640 ms. It is possible to see the exponential decay in time of the signal. The region where dose is deposited (Bragg peak) looks darker as the signal decays faster due to an increase of R2 induced by polymerization.

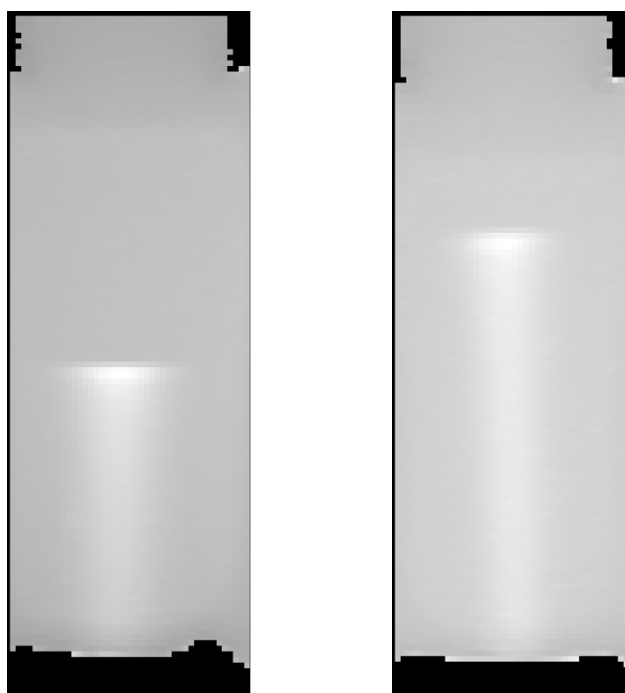


Figure 28. The output of Matlab algorithm is an R2 map whose values are graphically represented in scale of grey. The pixel is brighter where the R2 value is higher, as is the case of the Bragg peak region. In the picture, the R2 maps for the phantoms irradiated with protons at 70 mm proton (left) and at 101 mm (right).

3.4 Data analysis

The statistical analysis and the fitting of the data were aimed at assessing the dosimetric quantities defined as follows:

- *Sensitivity* (S), defined as the slope of the linear curve fitting the dose values against the instrument response. In optical measurements, the sensitivity S_{op} is expressed in $\text{Gy}^{-1}(\text{Abs}/\text{Dose})$, whereas in MRI analysis S_{MRI} units are $\text{Gy}^{-1}\text{s}^{-1}(\text{R2}/\text{Dose})$.
- *Dose Resolution* ($D_{\Delta}^{95\%}$), introduced in section 1.3 as the minimal detectable dose difference with a given level of confidence, p . Starting from Eq. (1.16), with a confidence level $p = 95\%$, the dose resolution can be defined for the optical and the MRI analysis as follows:

$$D_{\Delta}^{95\%} = 2.77 \frac{\sigma_{Abs}}{S_{op}} \quad (3.1a)$$

$$D_{\Delta}^{95\%} = 2.77 \frac{\sigma_{R2}}{S_{MRI}} \quad (3.1b)$$

where σ_{Abs} and σ_{R2} are the standard deviation of the optical absorbance and the R2 relaxation rate of the irradiated samples.

- *Precision* ($Pres$), it describes the relative dispersion between independent measurement results of the dosimeters irradiated at the same dose. It is given by the ratio of the standard deviation of the irradiated specimen response and their mean value:

$$Pres = \frac{\sigma_{Abs}}{Abs} \quad (3.2a)$$

$$Pres = \frac{\sigma_{R2}}{\overline{R2}} \quad (3.2b)$$

where σ_{Abs} and σ_{R2} are the same as above, while \overline{Abs} and $\overline{R2}$ are the mean value of the optical absorbance and the R2 relaxation rate.

- *Accuracy* (Accur), it evaluates the relative difference between the measured dose compared to the prescribed one:

$$Accur = \frac{D_{eval} - D_{ref}}{D_{ref}} \quad (3.3)$$

where D_{ref} is the prescribed dose value and D_{eval} is the dose value evaluated from the instrument response based on the calibration curve.

4. Results and discussion

The main experimental results obtained throughout the several analyses of the PAGAT gel dosimeters will be presented in this chapter. The dosimetric quantities introduced beforehand will be reported for each characterization test and the temporal evolution of the optical signals will be presented to discuss their temporal stability.

The volumetric response of the phantoms will be reported comparing it with the dose profiles measured with ionization chambers and gafchromic films. The issue of high-LET quenching effect will be examined.

The experimental data will be given in graphs and tables with one standard deviation of uncertainty.

4.1 Characterization

The purpose of this phase was to verify a linear dose response and calculate dosimetric parameters such as sensitivity, linearity range and accuracy, with respect to various irradiation conditions. Spectrophotometric cuvettes were irradiated using both protons and carbon ions to examine any potential dependence on the LET. The energy dependence was investigated irradiating with protons at two different energies. As a reference, at least four cuvettes were kept non-irradiated in each batch for blank subtraction. The dosimetric performance was evaluated with both spectrophotometric and MRI measurements.

The temporal evolution of the dose response was assessed by conducting spectrophotometric analysis at five different times after irradiation: the first

measurement was taken 2 days post-irradiation, the second after one week, the third after around 2 weeks, the fourth after 3 weeks and the last after more than two months.

4.1.1 Spectrophotometric analysis

The preliminary optical response of the characterization samples irradiated with protons and carbon ions was recorded through spectrophotometric measurements and is summarized in Figure 29.

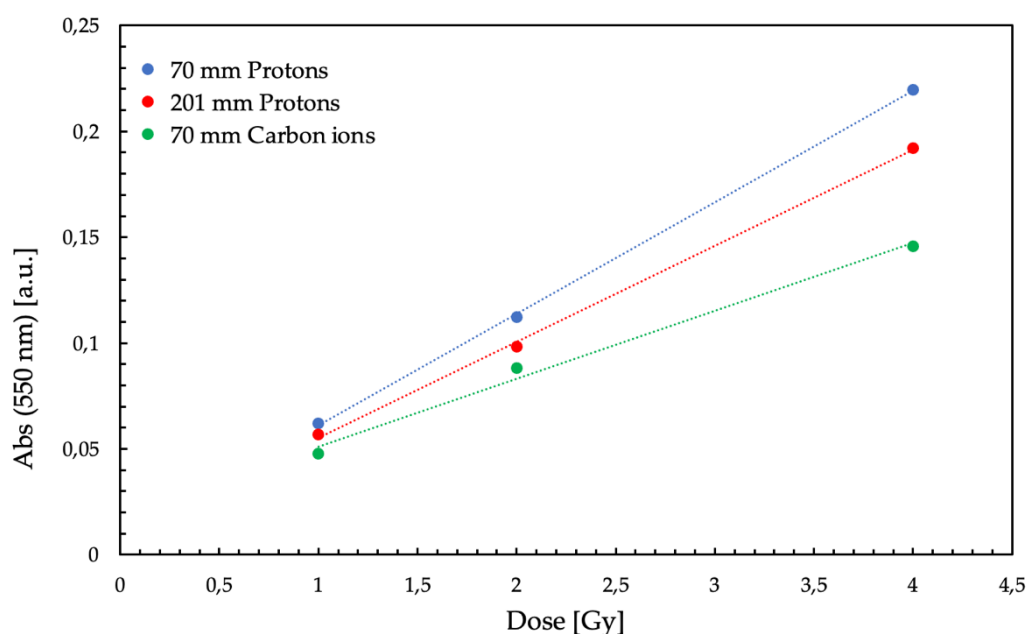


Figure 29. Optical response comparison of the characterization tests. Data were acquired 3 days after irradiation. Linear fitting curves are shown through the dotted lines and error bars are not represented for an easier visualization. Uncertainties range from 0.002 to 0.02.

A good linearity of the response was confirmed for the entire range of inspected doses. The curves are statistically very similar and this provides evidence that the optical response is relatively unaffected by energy or LET dependences. However, it is worth noticing a slight decrease in sensitivity as the proton energy rises and as the LET increases from proton to carbon ions.

In Table 8, the dosimetric quantities extrapolated from results of the optical analysis are summarized. Dose resolutions of less than 1 Gy for all tests were found in

accordance with previous studies, while a mean accuracy of the order of 1-2% was achieved. Sensitivity values are also comparable with those obtained with the same analysis by an earlier investigation focusing on the use of polymerization inhibitors on PAGAT dosimeters [60]. Mean precisions of the order of 10% are attributable to standard deviations larger than those found in previous studies, the reason of which may be due to uncertainties linked to the fabrication process.

Table 8. Dosimetric parameters obtained through optical analysis at $\lambda = 550$ nm. Precision and accuracy values are computed as an average of the single sample measurements. The mean value of the accuracy was calculated considering the absolute values of the single measurements.

	70 mm Protons	201 mm Protons	70 mm Carbon ions
Sensitivity [Gy^{-1}]	0.0527 \pm 0.0009	0.0454 \pm 0.0013	0.0321 \pm 0.0029
Dose Resolution [Gy]	0.138	0.823	0.493
Precision [%]	2.49	12.40	9.27
Accuracy [%]	1.2 \pm 0.9	2.1 \pm 1.5	6.5 \pm 4.5

The temporal stability of the optical response was evaluated by considering the evolution of the sensitivity throughout a period of more than two months after irradiation. The analyzed samples were uniformly irradiated at different doses using protons of 70 mm energy and their readout post irradiation was repeated five times: after 2 days, one week (7 days), two weeks (12 days), three weeks (21 days) and two months and a half (75 days). The time evolution of the sensitivity is presented in the plot of Figure 30. As expected by previous studies, a good temporal stability was confirmed: all optical sensitivity values lie within a $\pm 1.5\%$ interval around 0.03 Gy^{-1} , except for the first one (+6.3% above 0.03 Gy^{-1}). The higher value associated to the first measurement can be related to incomplete post-irradiation polymerization and therefore a dosimeter response not fully developed yet after two days.

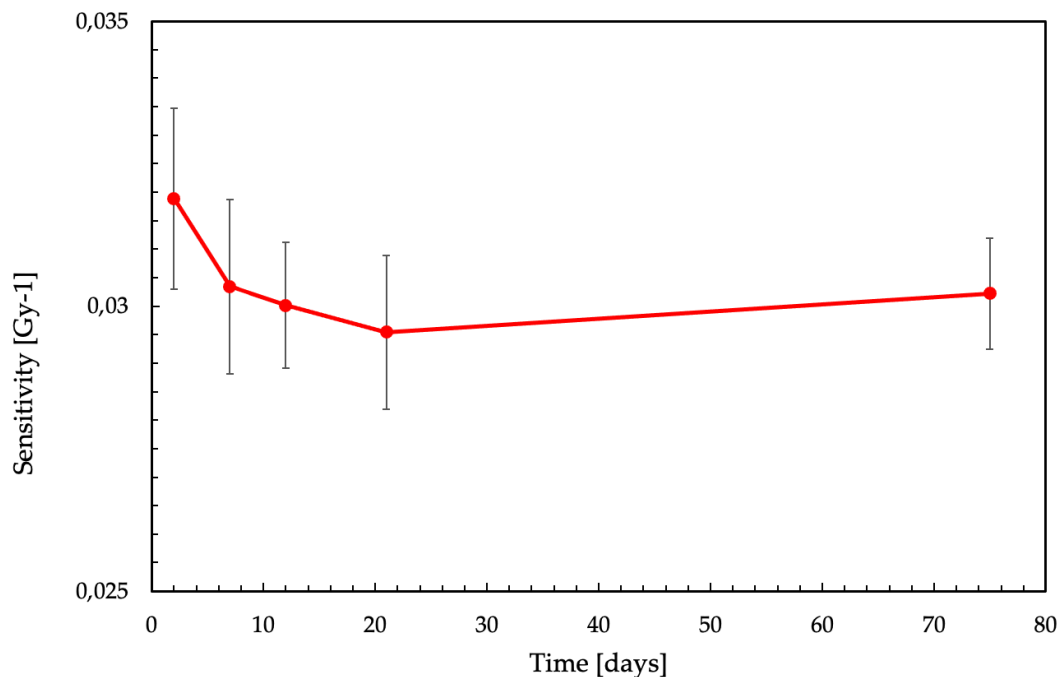


Figure 30. Temporal evolution over a period of about two months of the optical sensitivity of PAGAT dosimeters uniformly irradiated at 1 Gy, 2 Gy and 4 Gy using 70 mm protons. Measurements were performed at $\lambda = 550$ nm.

The stability analysis of the PAGAT dosimeters irradiated using protons shows comparable results to the ones attained irradiating the gels with photons or electrons. There is evidence to assume that the particle-type does not affect the stability properties of these dosimeters and, for this reason, the behaviour in time of the signal recorded by gels irradiated with carbon ions is expected to show a similar trend.

4.1.2 MRI analysis

The cuvettes were then analyzed with the use of MRI measurements in order to characterize the performance of the gel also through this technique. The characterization samples were scanned by means of a multiple spin-echo sequence featuring 32 TE and consequently a series of 32 T2-weighted images was obtained. These images were then processed using the Matlab code described beforehand thanks

to which an R2 map was extracted. The output of this elaboration is shown in Figure 31 where the R2 map is graphically rendered in a scale of grey.

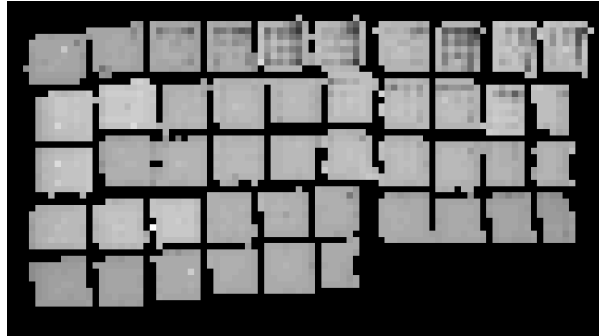


Figure 31. Output of the Matlab algorithm returning an R2 map in scale of grey for the cuvettes. The rectangular shapes are generated by the signal resulting from cuvettes sliced perpendicular to their vertical axis.

A relevant number of pixels from each cuvette area was selected and the mean R2 values were computed. The statistical analysis was subsequently conducted resulting in the characterization curves plotted in Figure 32.

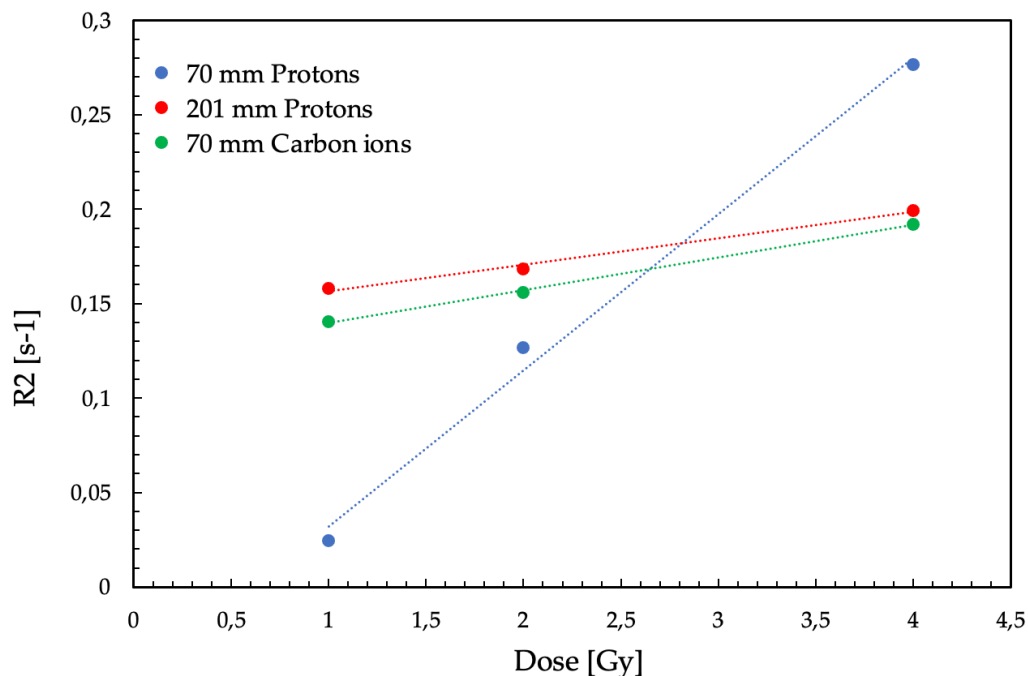


Figure 32. R2 response comparison of the characterization tests. Data were acquired 6 days after irradiation. Linear fitting curves are shown through the dotted lines and error bars are not represented for an easier visualization. Uncertainties range from 0.009 to 0.041 s⁻¹.

Good linearity was confirmed also for MRI analysis for the entire range of inspected doses. While the curves of samples irradiated with 201 mm protons and 70 mm carbon ions are statistically very similar, the one associated to 70 mm protons shows a different sensitivity suggesting a potential energy or LET dependence. The difference might be however partly attributed to a low resolution of the MRI acquisition. As can be seen in Figure 31, the R2 map is affected by noise especially in the upper part of the image where cuvettes for the 70 mm protons irradiation are scanned. An MRI sequence optimization could be useful to improve on this issue.

Similarly to what done in the optical analysis, dosimetric quantities were extrapolated from R2 values and are summarized in Table 9. Dose resolution of less than 1 Gy was found for the 70 mm protons test comparable to what obtained in the optical response, while for 201 mm protons and 70 mm carbon ions irradiations the dose resolution resulted around 3.5 Gy. Such values for the resolution are due to the lower sensitivities characterizing the last two irradiation tests. Mean accuracy values are also higher compared the ones obtained with optical measurements, even though they remain below 7%. Mean precision values are higher than 10% for all three cases, with the value for the 70 mm protons around 20% due to large standard deviations which can be attributed to the noise present in the R2 map.

Table 9. Dosimetric parameters obtained through MRI analysis. Precision and accuracy values are computed as an average of the single sample measurements. The mean value of the accuracy was calculated considering the absolute values of the single measurements.

	70 mm Protons	201 mm Protons	70 mm Carbon ions
Sensitivity [Gy ⁻¹ s ⁻¹]	0.0828±0.0067	0.0140±0.0013	0.0173±0.0006
Dose Resolution [Gy]	0.596	3.687	3.477
Precision [%]	20.61	10.64	13.35
Accuracy [%]	5.9±4.2	6.7±4.8	2.6±1.9

4.2 Volumetric response

The analysis on the cylindrical phantoms was aimed at assessing the volumetric response of the gels both in terms of dose profiles along the direction of irradiation and transversal dose distributions perpendicular to it. Three phantoms were irradiated using single-spot beams, two with protons at 70 mm and 101 mm, and one with carbon ions at 90 mm. The dose distribution recorded in the gels was extracted through MRI scanning of the phantoms conducted at least 6 days after irradiation in order to allow the polymeric response to fully develop.

The MRI readout consisted in a multiple spin echo sequence of different slices of the phantoms with 32 TE for each slice, as described beforehand. The T2-weighted images were elaborated using the Matlab algorithm in order to retrieve the corresponding R2 maps, similarly to what has been done for the characterization samples. The Matlab outputs for the three phantoms are given in Figure 33.

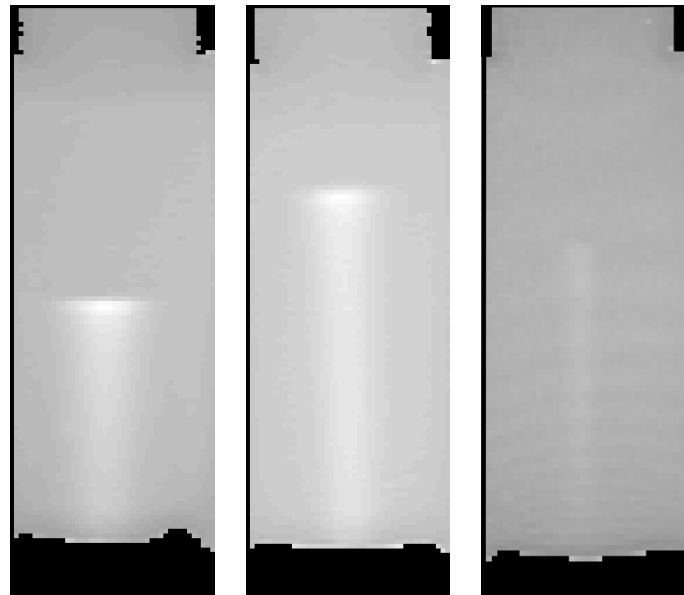


Figure 33. Output of the Matlab algorithm returning an R2 map in scale of grey for the cylindrical phantoms sliced along their vertical axis. R2 map from the 70 mm proton beam (left), from the 101 mm proton beam (centre) and 90 mm carbon ion beam (right). It is possible to appreciate the difference in lateral diffusion between carbon ion beam and proton beam.

The phantoms were scanned with slices parallel to the cylinder axis and hence to the beam direction. To extract the depth-dose profiles from the spatial distributions developing along the whole slice, pixels in the axial region of the R2 map were selected and their R2 values properly averaged. The experimental curves show therefore the dose profile (Bragg peak) against the depth in the beam direction. The peaks measured with PAGAT gel dosimeters were compared with reference profiles acquired using ionization chambers in water. The curves were normalized to have the peaks of the reference profiles correspond to 1, that is 100% of the signal, and in this way the quenching effect could be easily quantified.

In Figure 34 and Figure 35, the depth-dose curves resulting from the irradiations with proton beams are reported, while Figure 36 exhibits the results of the irradiation with carbon ion beam.

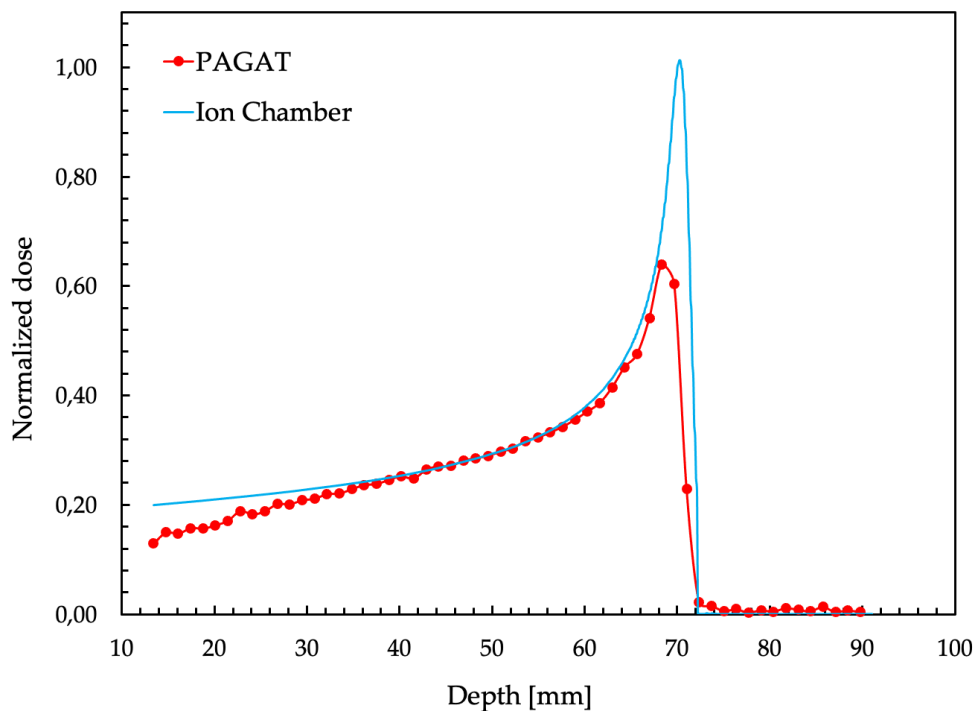


Figure 34. Normalized depth-dose profile for 70 mm (97.54 MeV) proton single-spot beam. The two curves were normalized at a depth of 50 mm.

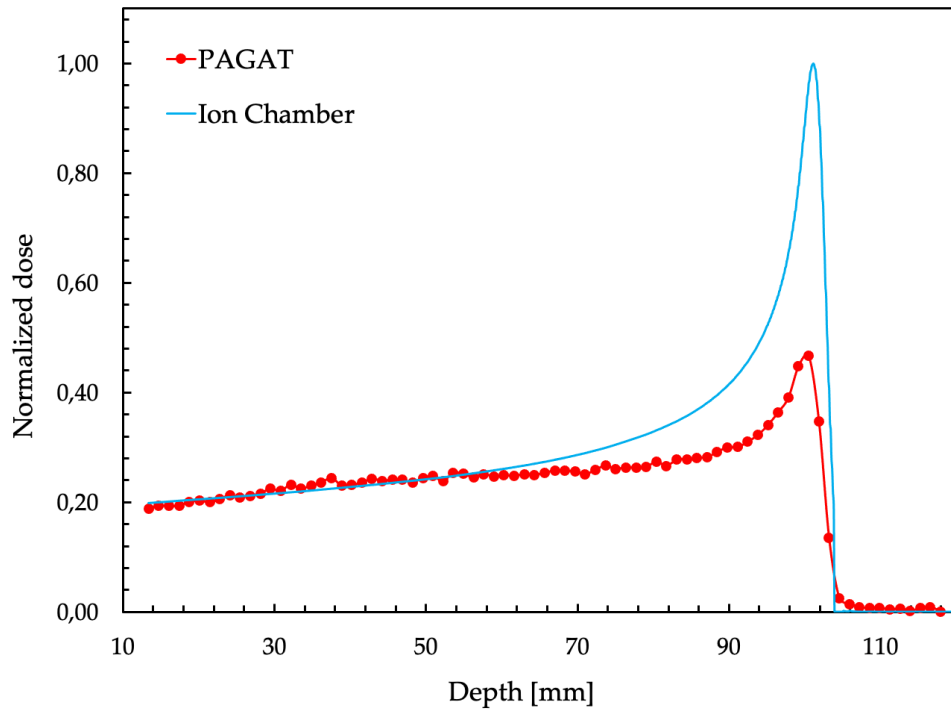


Figure 35. Normalized depth-dose profile for 101 mm (118.20 MeV) proton single-spot beam. The two curves were normalized at a depth of 50 mm.

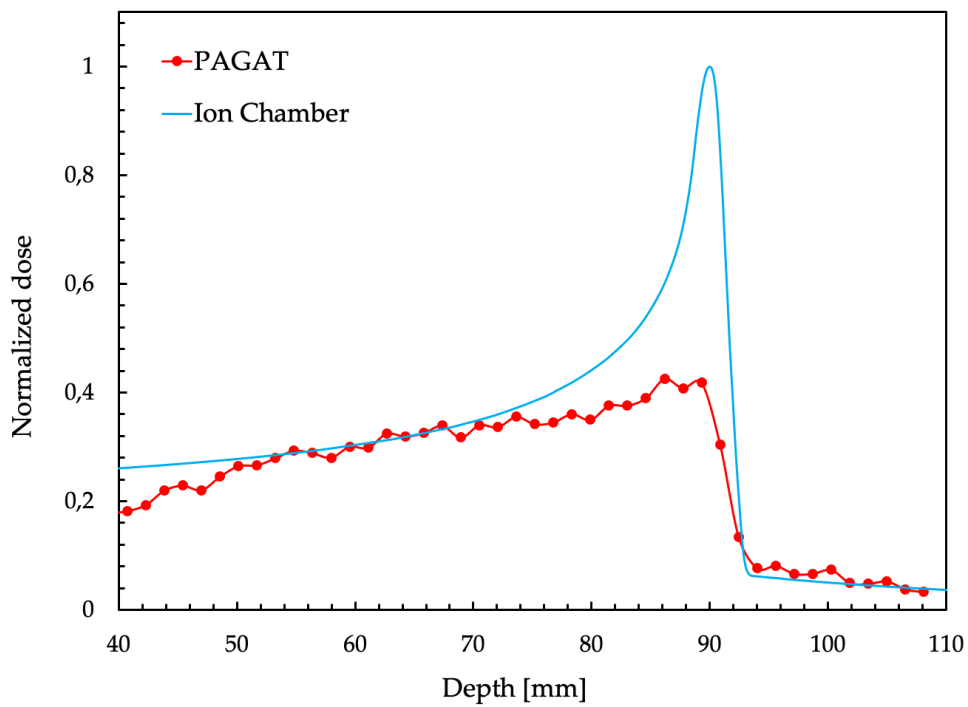


Figure 36. Normalized depth-dose profile for 90 mm (208.58 MeV/u) carbon ion single-spot beam. The two curves were normalized at a depth of 60 mm.

In the case of 70 mm proton irradiation (Figure 34), the agreement between the depth-dose profiles measured using PAGAT gel and ion chamber is good at the plateau and the first part of the Bragg peak, up to a depth of approximately 67 mm. A slight underestimation of the signal is observable at the beginning of the plateau between 10 mm and 30 mm depth, with an initial 5% difference which gradually reduces as the distance increases. At the Bragg peak, however, the gel underestimates the absorbed dose of approximately 35% compared to the reference profile. This under-response confirms the presence of a quenching effect due to LET increase in the distal part of the peak as expected from literature results. A very good agreement is found for what concerns the position of the peak in the two curves.

The 101 mm proton irradiation (Figure 35) shows a measured depth-dose profile which agrees very well to the reference one in the plateau region up to approximately 60 mm depth. Differently from the previous case, the quenching effect is relevant already in the first part of the peak and the underestimation at the Bragg peak is of the order of 55%. The LET dependence of the dosimeter sensitivity appears to be affected by the extraction energy of the particles. Similarly to the 70 mm proton irradiation, also in this second case the geometrical information is well recorded, with only +0.6 mm difference between the end-points of the two profiles.

The profile generated by the 90 mm carbon ion irradiation (Figure 36) shows similar characteristics to the previous ones. Similarly to the 70 mm proton profile, the plateau is slightly underestimated at its beginning with an initial 8% shortfall at 40 mm depth. From 50 mm on, the acquired curve follows well its reference up to approximately 75 mm, after which the quenching effect becomes relevant as the LET increases at higher depths. The underestimation at the Bragg peak is around 60%, the largest of all three cases. The dose tail in the distal part of the ion depth-dose curve, which is due to projectile fragmentation, is recorded with very good agreement both

from a quantitative point of view and a geometrical one, as the position of the peak and its tail are well recorded.

The overall results achieved with this analysis confirm what has been found in literature studies. An under-response of the PAGAT gel is observed at the Bragg peak as the LET increases with depth. The magnitude of this underestimation appears to be energy dependent, as the 101 mm proton irradiation shows higher quenching (55% shortfall) compared to the 70 mm proton one (35%). As expected, the gel response at the Bragg peak for the 90 mm carbon ion profile is the smallest (60% underestimation) since the LET of carbon ions is larger than the one of protons and hence the gel sensitivity is lower. Good agreement between the gel and the reference curve at the plateau of the depth-dose profile and at the fragmentation tail for carbon ions confirms that the gel dose response is not altered for low-LET values. The issue of LET-dependent gel sensitivity and corresponding quenching of the signal at high depths makes a quantitative measurement of the absolute dose very difficult with these polymeric gel devices. Nonetheless, the PAGAT dosimeter shows promising characteristics for what concerns the extrapolation of geometrical information as for all acquired curves the depths of the Bragg peaks are in very good agreement with the expected values. This characteristic could prove very useful for non-absolute dosimetry in profile verification for HT, where the dose deposition shows a finite range and the knowledge and control of it guarantees the efficacy of the treatment and the sparing of healthy tissues.

In addition to the depth-dose profile evaluation, the volumetric response of the phantoms was investigated considering the dose distribution developing on transversal planes perpendicular to the beam direction. Analogously to what described beforehand, the R2 maps obtained from the Matlab code were sampled by properly averaging the R2 values of pixels taken along directions perpendicular to the

cylinder axis and the resulting distributions were benchmarked with experimental profiles recorded by gafchromic films used for routine calibration of the beams. The irradiation of these films is performed in air, that is with no interface medium between the beam and the film, and for this reason the transversal dose profiles of the gels were taken along planes located at the bottom of the cylinders from which the beams entered the phantoms. The results of this analysis are shown in Figure 37, Figure 38, Figure 39 and in Table 10, where, due to the finite dimensions of the MRI voxels, all values are affected to spatial uncertainty comparable to half the voxel size.

Table 10. FWHM values comparison for gel dosimeters and gafchromic films. These values are computed from the profiles shown in the figures below. Linear interpolation between adjacent points was performed to find the value of the width at 50% height of the profiles.

FWHM	70 mm Protons	101 mm Protons	90 mm Carbon ions
PAGAT gel	15.9 mm	13.2 mm	7.3 mm
Gafchromic film	15.8 mm	13.7 mm	6.6 mm

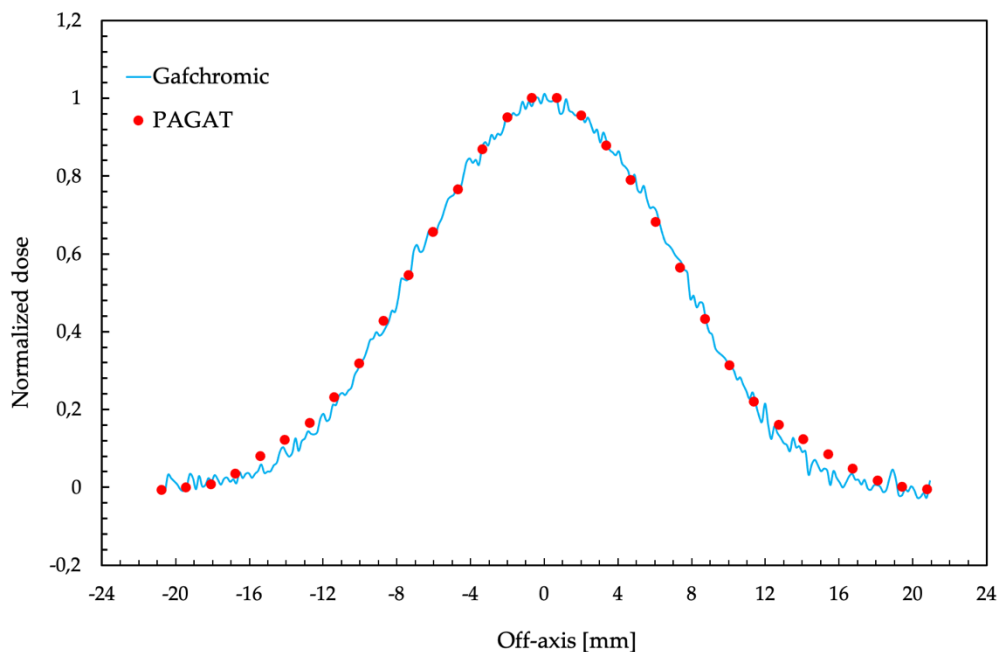


Figure 37. Transversal dose distribution for 70 mm proton single-spot beam. The two curves were normalized to their value at 0 mm off-axis. The gel profile was sampled at approximately 15 mm depth from the bottom of the phantom.

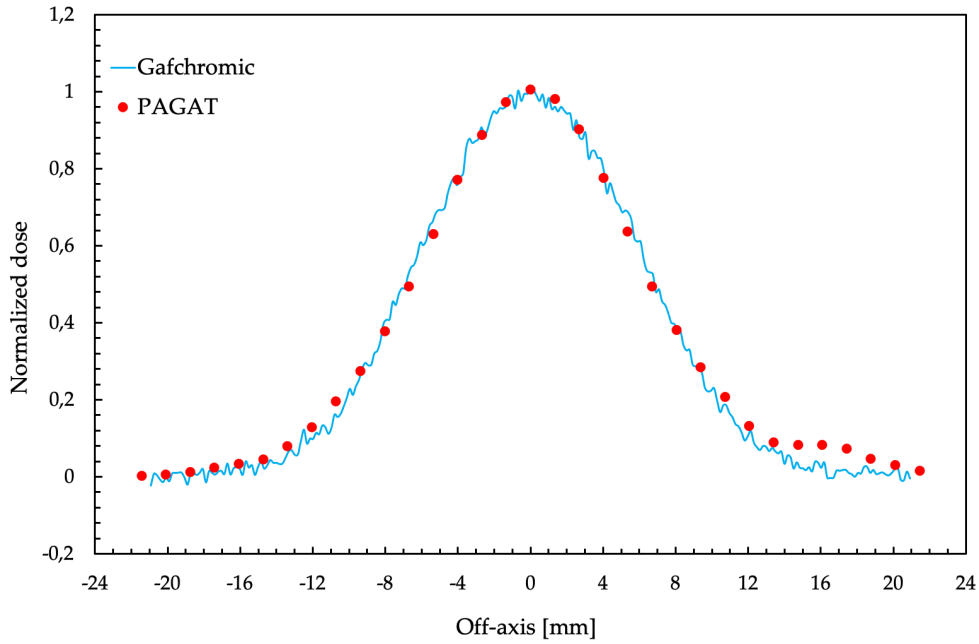


Figure 38. Transversal dose distribution for 101 mm proton single-spot beam. The two curves were normalized to their value at 0 mm off-axis. The gel profile was sampled at approximately 20 mm depth from the bottom of the phantom.

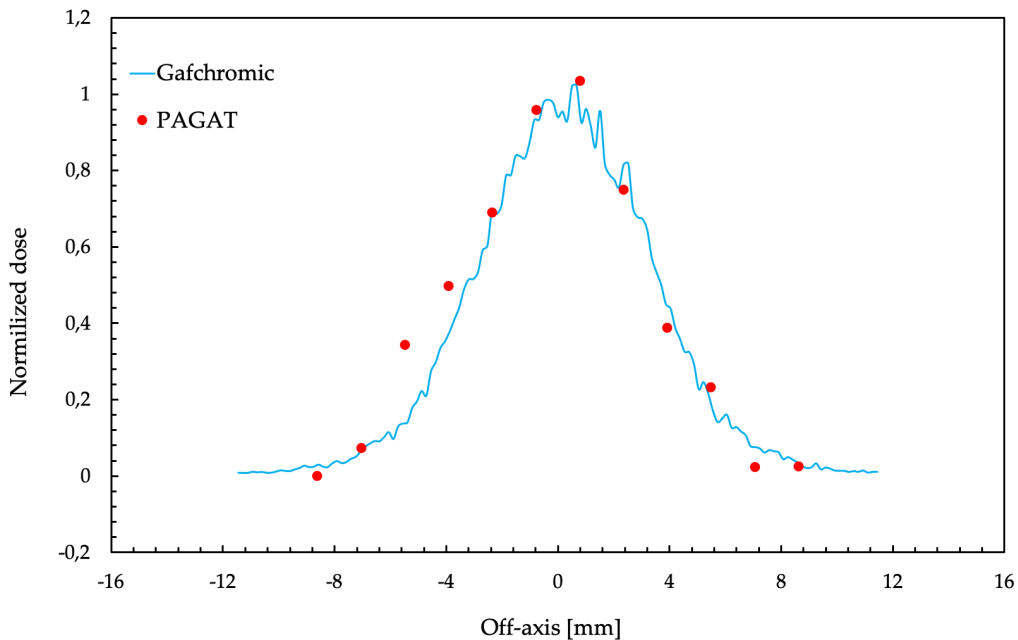


Figure 39. Transversal dose distribution for 90 mm carbon ion single-spot beam. The two curves were normalized to their value at 0 mm off-axis. The gel profile was sampled at approximately 40 mm depth from the bottom of the phantom.

This further analysis on the transversal distributions confirms what has been found during the investigation of the depth-dose profiles. The gel system shows a very good performance in recording the geometrical information of the dose distribution, as the agreement between the curves is extremely good. The main differences are observed in the 90 mm carbon ion distribution, where FWHM recorded by the gel is approximately 10% larger than the one obtained by the gafchromic film. Nonetheless, this is likely due to noise contributions in the MRI images which become more relevant in the carbon ion case as the corresponding dose profile is much smaller in width compared to the proton irradiations. Besides, the finite spatial resolution of the MRI analysis, which in carbon ion case is of the same order of magnitude of the profile FWHM, may contribute to the observed discrepancy. As a matter of fact, the FWHM difference for the proton distributions is around -3.5% for 101 mm case and 0.7% for the 70 mm one. The fact that transversal profiles do not show any under-response due to quenching effect confirms again that for low-LET values at the initial part of the depth-dose profile the gel dose response is not altered.

5. Conclusion and future development

The focus of this thesis was to analyze the dose response of PAGAT gel dosimeters in Hadron Therapy. The use of polymeric gel systems has shown great potential for the verification of dose profiles in Bragg-peak dominated hadronic irradiations as the three-dimensional nature of these gels allows for an ideal infinite spatial resolution, limited only by the performance of the measuring instrument. Additionally, unlike other chemical gel systems, polymeric gel response is unaffected by diffusion of the spatial information resulting in a temporal stability of the recorded signal for months after irradiation.

During the characterization phase, using 5 mL cuvette samples, good linearity was observed in both spectrophotometric and MRI measurements for investigated doses up to 4 Gy. The optical analysis revealed slight energy and LET dependences for the sensitivity, while the MRI measurements highlighted the need for pulse sequence optimization to improve the SNR and eventually the dose resolution and precision. The optical analysis of the characterization samples resulted in an average precision of 8%, a mean dose resolution of 0.48 Gy, and an average accuracy of 3%. For MRI measurements, the average precision was 15%, the mean dose resolution 2.59 Gy, and the average accuracy was 5%. These average values were calculated considering the different irradiation conditions.

Volumetric dose mapping conducted on cylindrical phantoms yielded excellent results for geometrical profile verification. The dimensions of the recorded dose deposition in terms of depth-dose curves and transversal distributions were in very good agreement with the reference profiles. The issue of high-LET quenching of the

signal was observed near the Bragg peak, leading to an underestimation of the normalized dose. This under-response was found to be influenced by the extraction energy of the particle and dependent on LET. The carbon ion irradiation exhibited the highest under-response at the peak, with a 60% shortfall compared to the reference profile, while the smallest amount of quenching was found for the lower energy proton irradiation with a 35% underestimation at the peak.

Future developments for the potential use of PAGAT dosimeters in HT should investigate and address the phenomenon of high-LET quenching of the dose response. One possible strategy to counteract this issue could be to construct LET calibration curves to correct the under-response of the gel at the Bragg peak. Alternatively, new gel compositions should be explored whose response show a lower dependence on LET. In this regard, particularly interesting are the results obtained with nanocomposite Fricke gel (NC-FG) dosimeters, prepared using nano-clay, perchloric acid and ferrous ions in deaerated conditions, whose sensitivity proved to be nearly constant at very high-LET values in the Bragg peak region [107]. Another area requiring further study consists in the definition of a standardized and optimized MRI sequence for the scanning of polymer gel dosimeter which would enable to fully exploit the 3D spatial dose resolution of these devices, especially by reducing imaging artefacts and improving SNR. Additionally, alternative gel compositions should be explored to reduce the toxicity of acrylamide-based dosimeters in order to ensure their safer handling for routine clinical usage.

Bibliography

- [1] World Health Organization, "Global Cancer Observatory," *International Agency for Research on Cancer*. [Online]. Available: <https://gco.iarc.fr>
- [2] J. M. Borrás *et al.*, "The impact of cancer incidence and stage on optimal utilization of radiotherapy: Methodology of a population based analysis by the ESTRO-HERO project," *Radiotherapy and Oncology*, vol. 116, no. 1, pp. 45–50, Jul. 2015, doi: 10.1016/j.radonc.2015.04.021.
- [3] K. Tanha, S. R. Mahdavi, and G. Geraily, "Comparison of CCC and ETAR dose calculation algorithms in pituitary adenoma radiation treatment planning; Monte Carlo evaluation," *J Radiother Pract*, vol. 29, no. 4, pp. 447–455, Apr. 2014, doi: 10.1017/S1460396914000211.
- [4] R. X. Huang and P. K. Zhou, "DNA damage response signaling pathways and targets for radiotherapy sensitization in cancer," *Signal Transduct Target Ther*, vol. 5, no. 1, Dec. 2020, doi: 10.1038/s41392-020-0150-x.
- [5] A. Afshar-Oromieh *et al.*, "Comparison of 68 Ga-DOTATOC-PET/CT and PET/MRI hybrid systems in patients with cranial meningioma: Initial results," *Neuro Oncol*, vol. 17, no. 2, pp. 312–319, Feb. 2015, doi: 10.1093/neuonc/nou131.
- [6] J. R. Stickel and S. R. Cherry, "High-resolution PET detector design: Modelling components of intrinsic spatial resolution," *Phys Med Biol*, vol. 50, no. 2, pp. 179–195, Jan. 2005, doi: 10.1088/0031-9155/50/2/001.
- [7] A. Nakamoto *et al.*, "Ultra-high-resolution CT urography: Importance of matrix size and reconstruction technique on image quality," *Eur J Radiol*, vol. 130, Sep. 2020, doi: 10.1016/j.ejrad.2020.109148.
- [8] D. Stucht, K. A. Danishad, P. Schulze, F. Godenschweger, M. Zaitsev, and O. Speck, "Highest resolution in vivo human brain MRI using prospective motion correction," *PLoS One*, vol. 10, no. 7, Jul. 2015, doi: 10.1371/journal.pone.0133921.
- [9] M. J. Gazda and L. R. Coia, *Principles of radiation therapy*. 2001.

- [10] S. J. van Hoof, P. v. Granton, and F. Verhaegen, "Development and validation of a treatment planning system for small animal radiotherapy: SmART-Plan," *Radiotherapy and Oncology*, vol. 109, no. 3, pp. 361–366, Dec. 2013, doi: 10.1016/j.radonc.2013.10.003.
- [11] E. Spezi and G. Lewis, "An overview of Monte Carlo treatment planning for radiotherapy," *Radiat Prot Dosimetry*, vol. 131, no. 1, pp. 123–129, 2008, doi: 10.1093/rpd/ncn277.
- [12] P. Dixon and B. O'sullivan, "Current Perspective Radiotherapy quality assurance: time for everyone to take it seriously," *Eur J Cancer*, vol. 39, pp. 423–429, 2002, [Online]. Available: www.ejconline.com
- [13] Y. De Deene, "Gel dosimetry for the dose verification of Intensity Modulated Radiotherapy Treatments," *Z.Nlcd. Phys*, vol. 12, pp. 77–88, 2002.
- [14] Y. De Deene, "Essential characteristics of polymer gel dosimeters," *J Phys Conf Ser*, vol. 3, pp. 34–57, Jan. 2004, doi: 10.1088/1742-6596/3/1/006.
- [15] D. A. Low, J. M. Moran, J. F. Dempsey, L. Dong, and M. Oldham, "Dosimetry tools and techniques for IMRT," *Med Phys*, vol. 38, no. 3, pp. 1313–1338, 2011, doi: 10.1118/1.3514120.
- [16] W. U. Lauba and T. Wong, "The volume effect of detectors in the dosimetry of small fields used in IMRT," *Med Phys*, vol. 30, no. 3, pp. 341–347, Mar. 2003, doi: 10.1118/1.1544678.
- [17] S. Devic, "Radiochromic film dosimetry: Past, present, and future," *Physica Medica*, vol. 27, no. 3, pp. 122–134, Jul. 2011, doi: 10.1016/j.ejmp.2010.10.001.
- [18] S. Devic *et al.*, "Accurate skin dose measurements using radiochromic film in clinical applications," *Med Phys*, vol. 33, no. 4, pp. 1116–1124, 2006, doi: 10.1118/1.2179169.
- [19] A. Rosenfeld, A. Wroe, M. Carolan, and I. Cornelius, "Method of Monte Carlo simulation verification in hadron therapy with non-tissue equivalent detectors," *Radiat Prot Dosimetry*, vol. 119, no. 1–4, pp. 487–490, Sep. 2006, doi: 10.1093/rpd/nci618.
- [20] G. S. Ibbott, "Applications of gel dosimetry," *J Phys Conf Ser*, vol. 3, pp. 58–77, Jan. 2004, doi: 10.1088/1742-6596/3/1/007.
- [21] B. Farhood, G. Geraily, and S. M. M. Abtahi, "A systematic review of clinical applications of polymer gel dosimeters in radiotherapy," *Applied Radiation and Isotopes*, vol. 143, pp. 47–59, Jan. 2019, doi: 10.1016/j.apradiso.2018.08.018.

- [22] M. Lepage and K. Jordan, "3D dosimetry fundamentals: Gels and plastics," *J Phys Conf Ser*, vol. 250, pp. 253–261, 2010, doi: 10.1088/1742-6596/250/1/012055.
- [23] J. A. Adamovics and R. J. Coakley, "Chemical dosimeters," *J Phys Conf Ser*, vol. 1305, no. 1, Aug. 2019, doi: 10.1088/1742-6596/1305/1/012028.
- [24] H. Fricke and S. Morse, "The chemical action of Roentgen rays on dilute ferrosulphate solutions as measure of dose," *Am. J. Roentgenol. Radium Therapy Nucl. Med.*, vol. 18, pp. 430–432, 1927.
- [25] L. J. Schreiner, "Review of Fricke gel dosimeters," *J Phys Conf Ser*, vol. 3, pp. 9–21, Jan. 2004, doi: 10.1088/1742-6596/3/1/003.
- [26] J. C. Goret, Y. S. Kangt, and R. J. Schulz, "Measurement of radiation dose distributions by nuclear magnetic resonance (NMR) imaging," *Phys Med Biol*, vol. 29, no. 10, pp. 1189–1190, 1984.
- [27] G. Gambarini, S. Arrigoni, M. C. Cantone, N. Molho, L. Facchielli, and A. E. Sichirollo, "Dose-response curve slope improvement and result reproducibility of ferrous-sulphate-doped gels analysed by NMR imaging," *Phys Med Biol*, vol. 39, pp. 703–717, 1994.
- [28] A. Un, "Water and tissue equivalency of some gel dosimeters for photon energy absorption," *Applied Radiation and Isotopes*, vol. 82, pp. 258–263, 2013, doi: 10.1016/j.apradiso.2013.09.002.
- [29] S. Brown *et al.*, "Radiological properties of the PRESAGE and PAGAT polymer dosimeters," *Applied Radiation and Isotopes*, vol. 66, no. 12, pp. 1970–1974, Dec. 2008, doi: 10.1016/j.apradiso.2008.06.005.
- [30] C. Baldock, P. J. Harris, A. R. Piercy, and B. Healy, "Experimental determination of the diffusion coefficient in two-dimensions in ferrous sulphate gels using the finite element method," *Australas Phys Eng Sci Med*, vol. 24, 2001.
- [31] M. Marrale and F. D'errico, "Hydrogels for three-dimensional ionizing-radiation dosimetry," *Gels*, vol. 7, no. 2, Jun. 2021, doi: 10.3390/gels7020074.
- [32] M. J. Maryanski, J. C. Gore, R. P. Kennan, and R. J. Schulz, "NMR relaxation enhancement in gels polymerized and cross-linked by ionizing radiation: new approach to 3D dosimetry by MRI," *Magn Reson Imaging*, vol. II, pp. 253–258, 1993.
- [33] C. Baldock, "Historical overview of the development of gel dosimetry: A personal perspective," *J Phys Conf Ser*, vol. 56, no. 1, pp. 14–22, Dec. 2006, doi: 10.1088/1742-6596/56/1/002.

- [34] C. Baldock *et al.*, "Polymer gel dosimetry," *Phys Med Biol*, vol. 55, no. 5, 2010, doi: 10.1088/0031-9155/55/5/R01.
- [35] M. J. Mayanski *et al.*, "Magnetic resonance imaging of radiation dose distributions using a polymer-gel dosimeter," *Phys Med Biol*, vol. 39, pp. 1437–1455, 1994.
- [36] C. Baldock *et al.*, "Experimental procedure for the manufacture and calibration of polyacrylamide gel (PAG) for magnetic resonance imaging (MRI) radiation dosimetry," *Phys Med Biol*, vol. 43, pp. 695–702, 1998.
- [37] S. M. Abtahi, "Characteristics of a novel polymer gel dosimeter formula for MRI scanning: Dosimetry, toxicity and temporal stability of response," *Physica Medica*, vol. 32, no. 9, pp. 1156–1161, Sep. 2016, doi: 10.1016/j.ejmp.2016.08.008.
- [38] P. M. Fong, D. C. Keil, M. D. Does, and J. C. Gore, "Polymer gels for magnetic resonance imaging of radiation dose distributions at normal room atmosphere," *Phys Med Biol*, vol. 46, no. 12, 2001.
- [39] Y. De Deene *et al.*, "A basic study of some normoxic polymer gel dosimeters," *Phys Med Biol*, vol. 47, pp. 3441–3463, 2002.
- [40] A. J. Venning, S. Brindha, B. Hill, and C. Baldock, "Preliminary study of a normoxic PAG gel dosimeter with tetrakis (hydroxymethyl) phosphonium chloride as an anti-oxidant," *J Phys Conf Ser*, vol. 3, pp. 155–158, Jan. 2004, doi: 10.1088/1742-6596/3/1/016.
- [41] R. J. Senden, P. De Jean, K. B. McAuley, and L. J. Schreiner, "Polymer gel dosimeters with reduced toxicity: A preliminary investigation of the NMR and optical dose-response using different monomers," *Phys Med Biol*, vol. 51, no. 14, pp. 3301–3314, Jul. 2006, doi: 10.1088/0031-9155/51/14/001.
- [42] J. W. T. Spinks and R. J. Woods, *An Introduction to Radiation Chemistry*, Third Edition. John Wiley & Sons, 1990.
- [43] C. Ferradini and J.-P. Jay-Gerin, "The effect of pH on water radiolysis: a still open question - Minireview," *Res. Chem. Intermed*, vol. 26, no. 6, pp. 549–565, 2000.
- [44] W. G. Burns, "Effect of Radiation Type in Water Radiolysis," *J. Chem. SOC., Faraday Trans. I*, vol. 77, pp. 2803–2813, 1981.
- [45] R. J. Young and P. A. Lovell, *Introduction to polymers*, Third Edition. Taylor & Francis Group, 1987.
- [46] D. I. Bower, *An Introduction to Polymer Physics*, First Edition. Cambridge University Press, 2002.

- [47] M. Wang, L. Guo, and H. Sun, "Manufacture of Biomaterials," *Encyclopedia of Biomedical Engineering*, vol. 1, pp. 116–134, 2019.
- [48] L. W. McKeen, "Introduction to Plastics and Polymers," *Fatigue and Tribological Properties of Plastics and Elastomers*, vol. 3, pp. 45–64, 2016.
- [49] X. Coqueret, *Radiation-induced polymerization*. 2017.
- [50] O. L. J. Virtanen *et al.*, "Direct Monitoring of Microgel Formation during Precipitation Polymerization of N-Isopropylacrylamide Using in Situ SANS," *ACS Omega*, vol. 4, no. 2, pp. 3690–3699, Feb. 2019, doi: 10.1021/acsomega.8b03461.
- [51] K. B. McAuley, "Fundamentals of polymer gel dosimeters," *J Phys Conf Ser*, vol. 56, no. 1, pp. 35–44, Dec. 2006, doi: 10.1088/1742-6596/56/1/004.
- [52] S. J. Hepworth, M. O. Leach, and S. J. Doran, "Dynamics of polymerization in polyacrylamide gel (PAG) dosimeters: (II) modelling oxygen diffusion," *Phys Med Biol*, vol. 44, pp. 1875–1884, 1999.
- [53] A. I. Jirasek, C. Duzenli, C. Audet, and J. Eldridge, "Characterization of monomer/crosslinker consumption and polymer formation observed in FT-Raman spectra of irradiated polyacrylamide gels," *Phys Med Biol*, vol. 46, pp. 151–165, 2001, [Online]. Available: www.iop.org/Journals/pbPII:S0031-9155
- [54] A. I. Jirasek and C. Duzenli, "Effects of crosslinker fraction in polymer gel dosimeters using FT Raman spectroscopy," *Phys. Med. Biol*, vol. 46, pp. 1949–1961, 2001, [Online]. Available: www.iop.org/Journals/pbPII:S0031-9155
- [55] M. Lepage, A. K. Whittaker, L. Rintoul, S. J. Å Bäck, and C. Baldock, "The relationship between radiation-induced chemical processes and transverse relaxation times in polymer gel dosimeters," *Phys. Med. Biol*, vol. 46, pp. 1061–1074, 2001, [Online]. Available: www.iop.org/Journals/pbPII:S0031-9155
- [56] M. Sedaghat, R. Bujold, and M. Lepage, "Severe dose inaccuracies caused by an oxygen-antioxidant imbalance in normoxic polymer gel dosimeters," *Phys Med Biol*, vol. 56, no. 3, pp. 601–625, Feb. 2011, doi: 10.1088/0031-9155/56/3/006.
- [57] A. Jirasek, M. Hilts, and K. B. McAuley, "Polymer gel dosimeters with enhanced sensitivity for use in x-ray CT polymer gel dosimetry," *Phys Med Biol*, vol. 55, no. 18, pp. 5269–5281, Sep. 2010, doi: 10.1088/0031-9155/55/18/002.
- [58] A. Jirasek, M. Hilts, C. Shaw, and P. Baxter, "Investigation of tetrakis hydroxymethyl phosphonium chloride as an antioxidant for use in x-ray computed tomography polyacrylamide gel dosimetry," *Phys Med Biol*, vol. 51, no. 7, pp. 1891–1906, Apr. 2006, doi: 10.1088/0031-9155/51/7/018.

- [59] V. Spěváček, K. Pilařová, J. Končecová, and O. Konček, "The influence of antioxidant THPC on the properties of polymer gel dosimeter," *Phys Med Biol*, vol. 59, no. 17, pp. 5141–5161, Sep. 2014, doi: 10.1088/0031-9155/59/17/5141.
- [60] G. Magugliani *et al.*, "Practical role of polymerization inhibitors in polymer gel dosimeters," in *Nuovo Cimento della Societa Italiana di Fisica C*, Italian Physical Society, Nov. 2020. doi: 10.1393/ncc/i2020-20147-7.
- [61] M. McJury, M. Oldham, M. O. Leach, and S. Webb, "Dynamics of polymerization in polyacrylamide gel(PAG) dosimeters: (I) ageing and long-term stability," *Phus. Med. Biol.*, vol. 44, pp. 1863–1873, 1999.
- [62] B. Farhood, G. Geraily, and S. M. M. Abtahi, "A systematic review of clinical applications of polymer gel dosimeters in radiotherapy," *Applied Radiation and Isotopes*, vol. 143, pp. 47–59, Jan. 2019, doi: 10.1016/j.apradiso.2018.08.018.
- [63] Y. De Deene, "Review of quantitative MRI principles for gel dosimetry," *J Phys Conf Ser*, vol. 164, 2009, doi: 10.1088/1742-6596/164/1/012033.
- [64] C. A. De Caro and H. Claudia, *UV/VIS Spectrophotometry-Fundamentals and Applications*. Mettler Toledo AG, 2015. [Online]. Available: <https://www.researchgate.net/publication/321017142>
- [65] L. Sommer, *Analytical absorption spectrophotometry in the visible and ultraviolet : the principles*. Elsevier, 1989.
- [66] F. S. Rocha, A. J. Gomes, C. N. Lunardi, S. Kaliaguine, and G. S. Patience, "Experimental methods in chemical engineering: Ultraviolet visible spectroscopy—UV-Vis," *Canadian Journal of Chemical Engineering*, vol. 96, no. 12, pp. 2512–2517, Dec. 2018, doi: 10.1002/cjce.23344.
- [67] G. Gambarini, G. Gomasasca, R. Marchesini, A. Pecci, L. Pirola, and S. Tomatis, "Three-dimensional determination of absorbed dose by spectrophotometric analysis of ferrous-sulphate agarose gel," *Nuclear Instruments and Methods in Physics Research A*, vol. 422, pp. 643–648, 1999.
- [68] K. H. Chang *et al.*, "Spectrophotometric determination of the optimal wavelength for a polymer-gel dosimeter," *Journal of the Korean Physical Society*, vol. 62, no. 8, pp. 1194–1198, Apr. 2013, doi: 10.3938/jkps.62.1194.
- [69] G. Gambarini *et al.*, "Optical analysis of gel dosimeters: Comparison of Fricke and normoxic polymer gels," *Nucl Instrum Methods Phys Res B*, vol. 263, no. 1 SPEC. ISS., pp. 191–195, 2007, doi: 10.1016/j.nimb.2007.04.085.
- [70] V. P. B. Grover, J. M. Tognarelli, M. M. E. Crossey, I. J. Cox, S. D. Taylor-Robinson, and M. J. W. McPhail, "Magnetic Resonance Imaging: Principles and

- Techniques: Lessons for Clinicians," *Journal of Clinical and Experimental Hepatology*, vol. 5, no. 3. Elsevier B.V., pp. 246–255, Sep. 01, 2015. doi: 10.1016/j.jceh.2015.08.001.
- [71] A. D. Elster, "Questions and Answers in MRI," *MRIquestions.com*. [Online]. Available: <https://mriquestions.com/index.html>
- [72] B. Mackiewich, "Basic principles of MRI," *Online Thesis on MRI by Blair Mackiewich*. 1995. Accessed: Apr. 12, 2023. [Online]. Available: <https://www.cs.sfu.ca/~stella/papers/blairthesis/main/node11.html>
- [73] G. B. Chavhan, P. S. Babyn, B. Thomas, M. M. Shroff, and E. Mark Haacke, "Principles, techniques, and applications of T2*-based MR imaging and its special applications," *Radiographics*, vol. 29, no. 5, pp. 1433–1449, Sep. 2009, doi: 10.1148/rg.295095034.
- [74] P. Sprawls, "Spin Echo Imaging Methods," *MAGNETIC RESONANCE IMAGING Principles, Methods, and Techniques*. Online Edition. Accessed: Apr. 14, 2023. [Online]. Available: <http://www.sprawls.org/mripmt/MRI06/index.html>
- [75] Y. De Deene and C. Baldock, "Optimization of multiple spin-echo sequences for 3D polymer gel dosimetry," *Phys. Med. Biol*, vol. 47, pp. 3117–3141, 2002.
- [76] S. Rossi, "Hadron Therapy Achievements and Challenges: The CNAO Experience," *Physics*, vol. 4, no. 1, pp. 229–257, Mar. 2022, doi: 10.3390/physics4010017.
- [77] A. Degiovanni and U. Amaldi, "History of hadron therapy accelerators," *Physica Medica*, vol. 31, no. 4, pp. 322–332, Jun. 2015, doi: 10.1016/j.ejmp.2015.03.002.
- [78] S. Braccini, "Scientific and technological development of Hadrontherapy," Sidlerstrasse 5, CH-3012 Bern, Switzerland, 2010.
- [79] PTCOG, "Particle Therapy Centres," *Particle Therapy Co-Operative Group*. Accessed: Apr. 25, 2023. [Online]. Available: <https://ptcog.site/index.php>
- [80] R. Wilson, "Radiological Use of Fast Protons," Cambridge, Massachusetts, 1946.
- [81] E. B. Podgoršak, *Radiation Physics for Medical Physicists*. Springer, 2005.
- [82] E. L. Alpen, "Quantities, Units, and Definitions," in *Radiation Biophysics*, Second Edition. Academic Press, 1998, pp. 1–10.
- [83] A. Blakely, F. Q. H. Ngo, S. B. Curtis, and C. A. Tobias, "Heavy-Ion Radiobiology: Cellular Studies," *Adv Radiat Biol*, vol. 11, pp. 295–389, 1984.
- [84] C. K. Ying, D. Bolst, L. T. Tran, S. Guatelli, A. B. Rosenfeld, and W. A. Kamil, "Contributions of secondary fragmentation by carbon ion beams in water

- phantom: Monte Carlo simulation," *J Phys Conf Ser*, vol. 851, no. 1, May 2017, doi: 10.1088/1742-6596/851/1/012033.
- [85] H. A. Bethe, "Moliere's Theory of Multiple Scattering," *Physical Review*, vol. 89, no. 6, pp. 1256–1266, 1953.
- [86] J. Ströbele, T. Schreiner, H. Fuchs, and D. Georg, "Comparison of basic features of proton and helium ion pencil beams in water using GATE," *Z Med Phys*, vol. 22, no. 3, pp. 170–178, Sep. 2012, doi: 10.1016/j.zemedi.2011.12.001.
- [87] W. T. Chu, "Overview of Light-Ion Beam Therapy," in *ICRU-IAEA meeting*, Berkeley (California), Mar. 2006, pp. 1–20.
- [88] E. M. Zeman, "Biologic Basis of Radiation Oncology," in *Clinical Radiation Oncology*, L. L. Gunderson and J. E. Tepper, Eds., Third Edition. 2012, pp. 3–42.
- [89] D. S. Chang, F. D. Lasley, I. J. Das, M. S. Mendonca, and J. R. Dynlacht, *Basic Radiotherapy Physics and Biology*. Springer, 2014.
- [90] J. Thariat *et al.*, "Hadrontherapy interactions in molecular and cellular biology," *Int J Mol Sci*, vol. 21, no. 1, Jan. 2020, doi: 10.3390/ijms21010133.
- [91] S. Doran, T. Gorjiara, A. Kacperek, J. Adamovics, Z. Kuncic, and C. Baldock, "Issues involved in the quantitative 3D imaging of proton doses using optical CT and chemical dosimeters," *Phys Med Biol*, vol. 60, no. 2, pp. 709–726, Jan. 2015, doi: 10.1088/0031-9155/60/2/709.
- [92] A. Jirasek and C. Duzenli, "Relative effectiveness of polyacrylamide gel dosimeters applied to proton beams: Fourier transform Raman observations and track structure calculations," *Med Phys*, vol. 29, no. 4, pp. 569–577, 2002, doi: 10.1118/1.1460873.
- [93] S. Al-Nowais, S. Doran, A. Kacperek, N. Krstajic, J. Adamovics, and D. Bradley, "A preliminary analysis of LET effects in the dosimetry of proton beams using PRESAGE™ and optical CT," *Applied Radiation and Isotopes*, vol. 67, no. 3, pp. 415–418, Mar. 2009, doi: 10.1016/j.apradiso.2008.06.032.
- [94] M. Valente *et al.*, "Linear energy transfer characterization of five gel dosimeter formulations for electron and proton therapeutic beams," *Applied Radiation and Isotopes*, vol. 178, Dec. 2021, doi: 10.1016/j.apradiso.2021.109972.
- [95] C. R. Baker, T. E. Quine, J. N. H. Brunt, and A. Kacperek, "Monte Carlo simulation and polymer gel dosimetry of 60 MeV clinical proton beams for the treatment of ocular tumours," *Applied Radiation and Isotopes*, vol. 67, no. 3, pp. 402–405, Mar. 2009, doi: 10.1016/j.apradiso.2008.06.031.

- [96] J. Heufelder, S. Stiefel, M. Pfaender, L. Lüdemann, G. Grebe, and J. Heese, "Use of BANG® polymer gel for dose measurements in a 68 MeV proton beam," *Med Phys*, vol. 30, no. 6, pp. 1235–1240, Jun. 2003, doi: 10.1118/1.1575557.
- [97] M. Hillbrand *et al.*, "Gel dosimetry for three dimensional proton range measurements in anthropomorphic geometries," *Z Med Phys*, vol. 29, no. 2, pp. 162–172, May 2019, doi: 10.1016/j.zemedi.2018.08.002.
- [98] H. Gustavsson, S. Å. J. Bäck, J. Medin, E. Grusell, and L. E. Olsson, "Linear energy transfer dependence of a normoxic polymer gel dosimeter investigated using proton beam absorbed dose measurements," *Phys Med Biol*, vol. 49, no. 17, pp. 3847–3855, Sep. 2004, doi: 10.1088/0031-9155/49/17/002.
- [99] T. Furuta *et al.*, "Comparison between Monte Carlo simulation and measurement with a 3D polymer gel dosimeter for dose distributions in biological samples," *Phys Med Biol*, vol. 60, no. 16, pp. 6531–6546, Aug. 2015, doi: 10.1088/0031-9155/60/16/6531.
- [100] M. Yoshioka *et al.*, "Examination of fundamental characteristics of a polymer gel detector in a proton beam irradiation," *Radiat Meas*, vol. 46, no. 1, pp. 64–71, Jan. 2011, doi: 10.1016/j.radmeas.2010.08.007.
- [101] S. Rossi, "The National Centre for Oncological Hadrontherapy (CNAO): Status and perspectives," *Physica Medica*, vol. 31, no. 4, pp. 333–351, Jun. 2015, doi: 10.1016/j.ejmp.2015.03.001.
- [102] "RW3 slab phantom," *ptwdosimetry.com*. Accessed: May 29, 2023. [Online]. Available: <https://www.ptwdosimetry.com/en/products/rw3-slab-phantom>
- [103] A. Pella *et al.*, "Commissioning and quality assurance of an integrated system for patient positioning and setup verification in particle therapy," *Technol Cancer Res Treat*, vol. 13, no. 4, pp. 303–314, 2014, doi: 10.7785/tcrt.2012.500386.
- [104] PerkinElmer, "Lambda 650, 800, and 950, Spectrophotometers." [Online]. Available: www.perkinelmer.com
- [105] Siemens, "MAGNETOM Skyra Fit Data Sheet." [Online]. Available: www.siemens.com/healthcare
- [106] Y. De Deene, R. Van De Walle, E. Achten, and C. De Wagter, "Mathematical analysis and experimental investigation of noise in quantitative magnetic resonance imaging applied in polymer gel dosimetry," *Signal Processing*, vol. 70, pp. 85–101, 1998.

- [107] T. Maeyama, N. Fukunishi, K. L. Ishikawa, K. Fukasaku, and S. Fukuda, "Radiological properties of nanocomposite Fricke gel dosimeters for heavy ion beams," *J Radiat Res*, vol. 57, no. 3, pp. 318–324, Jun. 2016, doi: 10.1093/jrr/rrw025.

List of Figures

Figure 1. Photograph of Fricke gel dosimeters irradiated up to 30 Gy at 5 Gy increments [31].	8
Figure 2. Photograph of PAGAT polymer gels irradiated at increasing doses from left to right.	9
Figure 3. Schematic representation of the interaction between different chemicals in a polymer gel dosimeter during the polymerization process, more specifically for an acrylamide-based dosimeter in a deoxygenated environment [22].	17
Figure 4. Chemical structure of AAm (a) and of Bis (b).	20
Figure 5. Chemical structure of THPC (a) and of THPO (b).	21
Figure 6. (left) [O ₂] versus time for gels with varying amounts of THPC. (right) [O ₂] versus time for samples consisting solely of deionized water and tap water [58].	22
Figure 7. Schematic of a UV-VIS spectrophotometer. The tungsten lamp is used as a source of visible light, while the deuterium lamp produces ultraviolet radiation. The spectrum generated by the lamps is continuous and is later made monochromatic by using a filter and a tunable monochromator [66].	25
Figure 8. Clinical MRI scanner	28
Figure 9. Graphical representation of the net magnetization vector as the averaged sum of the magnetic dipole moments of the single hydrogen nuclei [71].	29
Figure 10. Time evolution of magnetization components during FID [71].	31
Figure 11. Spin Echo process showing the use of a 180° pulse to rephase the proton spins and produce an echo event for the measurement of T ₂ [74].	33
Figure 12. Multiple spin-echo sequence for the acquisition of a dose image with MRI measurement [75].	37

- Figure 13.** Model of the layout of the CNAO synchrotron. The diameter of the synchrotron is about 25 m [76]. 43
- Figure 14.** Energy deposition in water by X-ray photons, protons and carbon ions. The energy of the X-rays is 21 MeV, the one of protons is 148 MeV and of carbon ions is 270 MeV/u [76]. 47
- Figure 15.** Top view on lateral dimension and energy deposition as function of range for a 200 MeV proton beam (left) and for a 200 MeV/A helium ion beam (right) [86]. 49
- Figure 16.** Lateral penumbra of a carbon beam compared to that of a proton beam with a similar range [87]. 49
- Figure 17.** RBE and OER vs LET: as LET increases, RBE reaches a maximum around 100 keV/ μm before it trends back down; OER decreases with LET until it reaches 1 at around 100 keV/ μm . Typical LET ranges for protons (P) and carbon ions (C) are also shown [89]. 52
- Figure 18.** (left) Relative depth dose curve for monoenergetic 133 MeV proton beam measured using MAGAT polymer gel dosimeter and silicon diode detector [98]. (right) Comparison between the measured depth-signal curve in PAGAT polymer gel dosimeter and the MC calculated depth-dose curve for 135 MeV/u carbon ion beam [99]. 55
- Figure 19.** Dose-signal curves measured at peak and entrance regions using PRESAGE (radiochromic) gel dosimeter irradiated with 60 MeV proton beam [91]. 55
- Figure 20.** The variation in LET as a function of depth for a monoenergetic proton beam (dashed curve, left-hand scale) and the measured relative sensitivity for the gel dosimeter (full curve, right-hand scale). Also shown is the depth-dose curve for the proton beam (dotted curve), normalized to 100% at the Bragg peak [98]. 56
- Figure 21.** Illustration of the spur model to clarify the energy (LET) dependence of the dose response. The solid arrow represents the single particle track, while the solid and dotted circles visualize the propagation of the spurs [100]. 57
- Figure 22.** Set of spectrophotometric cuvettes containing PAGAT gel composition. External dimensions: 11 x 11 x 50 mm. 61
- Figure 23.** Volumetric cylindrical phantom containing PAGAT gel composition next to three spectrophotometric cuvettes as comparison. External phantom dimensions: 75 mm base diameter, 134 mm height to the shoulder, 57 mm lid diameter, 165 mm total height. 61

- Figure 24.** (left) Irradiation set-up for the cuvettes using the vertical beamline. (right) RW3 layer support for the uniform dose irradiation of a group of four cuvettes. 62
- Figure 25.** (left) LAMBDA 650 UV/Vis spectrophotometer; (right) sample and reference holders insides the instrument. 64
- Figure 26.** Phantom in the automatized bed for MRI scanning..... 65
- Figure 27.** Five T2-weighted images at different TE times of the phantom irradiated with protons at 70 mm. From 1 to 5, the TE are equal to: 20 ms, 180 ms, 320 ms, 520 ms and 640 ms. It is possible to see the exponential decay in time of the signal. The region where dose is deposited (Bragg peak) looks darker as the signal decays faster due to an increase of R2 induced by polymerization. 67
- Figure 28.** The output of Matlab algorithm is an R2 map whose values are graphically represented in scale of grey. The pixel is brighter where the R2 value is higher, as is the case of the Bragg peak region. In the picture, the R2 maps for the phantoms irradiated with protons at 70 mm proton (left) and at 101 mm (right). 67
- Figure 29.** Optical response comparison of the characterization tests. Data were acquired 3 days after irradiation. Linear fitting curves are shown through the dotted lines and error bars are not represented for an easier visualization. Uncertainties range from 0.002 to 0.02..... 71
- Figure 30.** Temporal evolution over a period of about two months of the optical sensitivity of PAGAT dosimeters uniformly irradiated at 1 Gy, 2 Gy and 4 Gy using 70 mm protons. Measurements were performed at $\lambda = 550$ nm. 73
- Figure 31.** Output of the Matlab algorithm returning an R2 map in scale of grey for the cuvettes. The rectangular shapes are generated by the signal resulting from cuvettes sliced perpendicular to their vertical axis..... 74
- Figure 32.** R2 response comparison of the characterization tests. Data were acquired 6 days after irradiation. Linear fitting curves are shown through the dotted lines and error bars are not represented for an easier visualization. Uncertainties range from 0.009 to 0.041 s⁻¹..... 74
- Figure 33.** Output of the Matlab algorithm returning an R2 map in scale of grey for the cylindrical phantoms sliced along their vertical axis. R2 map from the 70 mm proton beam (left), from the 101 mm proton beam (centre) and 90 mm carbon ion beam (right). It is possible to appreciate the difference in lateral diffusion between carbon ion beam and proton beam. 76
- Figure 34.** Normalized depth-dose profile for 70 mm (97.54 MeV) proton single-spot beam. The two curves were normalized at a depth of 50 mm..... 77

- Figure 35.** Normalized depth-dose profile for 101 mm (118.20 MeV) proton single-spot beam. The two curves were normalized at a depth of 50 mm. 78
- Figure 36.** Normalized depth-dose profile for 90 mm (208.58 MeV/u) carbon ion single-spot beam. The two curves were normalized at a depth of 60 mm. 78
- Figure 37.** Transversal dose distribution for 70 mm proton single-spot beam. The two curves were normalized to their value at 0 mm off-axis. The gel profile was sampled at approximately 15 mm depth from the bottom of the phantom. 81
- Figure 38.** Transversal dose distribution for 101 mm proton single-spot beam. The two curves were normalized to their value at 0 mm off-axis. The gel profile was sampled at approximately 20 mm depth from the bottom of the phantom. 82
- Figure 39.** Transversal dose distribution for 90 mm carbon ion single-spot beam. The two curves were normalized to their value at 0 mm off-axis. The gel profile was sampled at approximately 40 mm depth from the bottom of the phantom. 82

List of Tables

Table 1. Different formulations for normoxic gel dosimeters [41].	10
Table 2. Radiochemical yields of products in the radiolysis of pure neutral water at room temperature with hard X-rays, gamma-rays or fast electrons [42]......	12
Table 3. Rate constants in mol ⁻¹ s ⁻¹ [34].	16
Table 4. PAGAT formulation. The % refers to weight percentage [40].	19
Table 5. Approximate values for T1 and T1 at 1.5T in different biological environments [71].	32
Table 6. Number of PT and CIRT facilities in clinical operation per country to April 2023 [79].	40
Table 7. PAGAT gel composition as used during the analysis. The % refers to weight percentage.....	59
Table 8. Dosimetric parameters obtained through optical analysis at $\lambda = 550$ nm. Precision and accuracy values are computed as an average of the single sample measurements. The mean value of the accuracy was calculated considering the absolute values of the single measurements.	72
Table 9. Dosimetric parameters obtained through MRI analysis. Precision and accuracy values are computed as an average of the single sample measurements. The mean value of the accuracy was calculated considering the absolute values of the single measurements.	75
Table 10. FWHM values comparison for gel dosimeters and gafchromic films. These values are computed from the profiles shown in the figures below. Linear interpolation between adjacent points was performed to find the value of the width at 50% height of the profiles.	81

List of Acronyms

<i>Abs</i>	Absorbance
<i>AAM</i>	Acrylamide
<i>AscA</i>	Ascorbic Acid
<i>BANANA</i>	Bis, Acrylamide, Nitrous oxide and Agarose
<i>Bis</i>	N,N'-methylene-bis-acrylamide
<i>BNCT</i>	Boron Neutron Capture Therapy
<i>CIRT</i>	Carbon Ion Radiation Therapy
<i>CT</i>	Computed Tomography
<i>FID</i>	Free-induction Decay
<i>FWHM</i>	Full Width at Half Maximum
<i>HT</i>	Hadron Therapy
<i>IMRT</i>	Intensity Modulated Radiation Therapy
<i>LET</i>	Linear Energy Transfer
<i>MAA</i>	Methacrylic Acid
<i>MAGAT</i>	Methacrylic Acid, Ascorbic acid, Gelatin and THPC
<i>MAGIC</i>	Methacrylic Acid, Ascorbic acid, Gelatin and Copper

<i>MC</i>	Monte Carlo simulation
<i>MRI</i>	Magnetic Resonance Imaging
<i>MU</i>	Monitor Unit
<i>NC-FG</i>	Nanocomposite Fricke Gel
<i>NIPAM</i>	N-isopropylacrylamide
<i>OER</i>	Oxygen Enhancement Ratio
<i>PAG</i>	Polyacrylamide gel
<i>PAGAT</i>	Polyacrylamide gel and THPC
<i>PET</i>	Positron Emission Tomography
<i>PT</i>	Proton Therapy
<i>QA</i>	Quality Assurance
<i>RBE</i>	Relative Biological Effectiveness
<i>RF</i>	Radiofrequency
<i>SOBP</i>	Spread Out Bragg Peak
<i>SE</i>	Spin Echo
<i>SNR</i>	Signal-to-noise Ratio
<i>TCT</i>	Transmission Computed Tomography
<i>TE</i>	Time to Echo
<i>THP</i>	Tris (hydroxymethyl) phosphine
<i>THPC</i>	Tetrakis (hydroxymethyl) phosphonium chloride
<i>THPO</i>	Tris (hydroxymethyl) phosphine oxide
<i>THPOH</i>	Tetrakis (hydroxymethyl) phosphonium hydroxide

<i>TLD</i>	Thermoluminescent Dosimeter
<i>TPS</i>	Treatment Planning System
<i>TR</i>	Repetition Time
<i>UV</i>	Ultraviolet
<i>VIS</i>	Visible light

